Advanced image processing and data analysis in optical coherence tomography of deep layers in the posterior segment of eye

Lian Duan
Doctoral Program in Applied Physics

Submitted to the Graduate School of
Pure and Applied Sciences
in Partial Fulfillment of the Requirements
for the Degree of Doctor of Philosophy in
Engineering

at the
University of Tsukuba

This thesis is dedicated to the memory of my grandmother ...

Contents

Abstract of dissertation **1**

1 Introduction **3**
- 1.1 Background 3
- 1.2 Aims of thesis 4
- 1.3 Thesis overview 4

2 Choroidal thickness measurement by PS-OCT **7**
- 2.1 Introduction 8
- 2.2 Image acquisition and enhancement 10
- 2.3 RPE/choroidal interface segmentation based on intensity contrast 10
- 2.4 Two-step CSI segmentation based on phase retardation contrast 12
  - 2.4.1 Rough segmentation 12
  - 2.4.2 Slope fitting in phase retardation 14
  - 2.4.3 Error correction 15
- 2.5 Results 16
  - 2.5.1 Performance of the CSI segmentation by PS-OCT 16
  - 2.5.2 Measurement of the choroidal thickness 20
- 2.6 Discussion 20
- 2.7 Summary 21

3 Enhanced visualization and characterization of the choroidal vessel by OCT **23**
- 3.1 Introduction and background 24
- 3.2 Choroidal volume extracting and flattening 26
- 3.3 Multi-scale adaptive thresholding based vessel segmentation 26
  - 3.3.1 Adaptive thresholding method 26
  - 3.3.2 Multi-scale adaptive thresholding based choroidal vessel segmentation 28
  - 3.3.3 Retinal vessel shadow rejection 31
- 3.4 Choroidal vasculature evaluation 32
  - 3.4.1 Choroidal vessel diameter estimation 32

3.4.2 Vascularized layer thickness measurement in the Choroid 33
3.5 *In vivo* application of choroidal vessel characterization algorithm 34
3.6 Discussion 38
3.7 Summary 40

4 Conclusion **43**

Appendices **45**

A Calibration Protocol for Resonalt Electro Optic Polarization Modulator **47**
A.1 Introduction and Purpose 47
A.2 Experimental Setup 47
A.3 Theory and Data Processing 48
A.4 Nonlinear Least Square Fitting 50
A.5 Experiment and Results 51
A.6 Summary 51

B Monte-Carlo-based phase retardation estimator for PS-OCT **53**
B.1 Background and purpose 53
B.2 Monte-Carlo-based phase retardation estimator 54
B.3 Performance evaluation 60
B.4 Summary 67

Acknowledgements **69**

Bibliography **70**

Curriculum vitae **81**

List of Figures

2.1 The efficiency of the Jones matrix averaging of 16 B-scans. (a) and (b) are the intensity image and phase retardation image extracted from single B-scan in PS-OCT, respectively. (c) and (d) are the intensity image and phase retardation image extracted from the average of 16 Jones matrix B-scans, respectively. 11

2.2 Segmentation of the RPE/choroid interface. 11

2.3 Illustration of rough segmentation flow. (a) Speckle reduced phase retardation image. (b) Distribution of second derivative in the B-scan image. (c) The node cost distribution of potential CSI are masked on the intensity OCT image. The yellow line shows the segmented RPE/choroid interface. (d) Rough segmentation result is shown in red. 13

2.4 Illustration of the slope fitting model in phase retardation. The black curve shows the phase retardation A-line signal marked with a white dashed line in Fig. 2.3(a) The blue and red dashed lines are the linear regression lines of phase retardation in the choroid and sclera, respectively. The CSI is determined by the intersection of these two lines. 14

2.5 The CSI obtained by fitting the phase retardation model shown in Fig. 2.4(a). The red curve shows the intersections of the linear regression lines in each A-scan, (b) The CSI smoothed by a median filter. 15

2.6 An example of intensity based segmentation error correction. The red and yellow lines denote the phase retardation based segmentation of the CSI and the intensity based correction result. 16

2.7 PS-OCT images of the macular region. (a) Intensity image, (b) Phase retardation image. The white line in (b) shows the CSI segmentation by phase retardation based segmentation. 17

2.8 A phase retardation based segmentation result is shown in intensity image (a) and phase retardation image (b). The yellow and black ellipses marked several unsmooth segments in the CSI. 18

2.9 An example of segmentation in an eye with low birefringence in some scleral region. The red and white lines show the segmentation result in intensity image (a) and phase retardation image (b), respectively. 19

2.10 Intensity (a) and phase retardation (b) B-scans acquired from an eye with poor visualization of the posterior choroidal region. The CSI segmentation results, a red line in (a) and a white line in (b), cannot represent the real CSI. 19

3.1 *En-face* slices extracted at (a) 25μm, (b) 100μm, (c) 175μm, and (d) 250μm under the RPE in the OCT volume flattened to the Bruch's membrane. 27

3.2 (a) OCT *en-face* slice. (b) Binary image obtained by adaptive local thresholding with a fixed window size. The white and black represent background and vessel, respectively. (c) Busyness distribution. (d) Result of artifact removal achieved by busyness filter. The light gray pixels are vessel artifact that is recognized and removed by busyness filter. 29

3.3 Choroidal vessel segmentation results corresponding to OCT *en-face* slices in Fig. 3.1. 31

3.4 (a) *En-face* projection of the hyper-reflective complex obtained by averaging the intensity values in each A-lines. (b) Vessel structure is enhanced by Frangi filter. (c) Retinal vessel shadow segmentation. 32

3.5 Choroidal vessel diameter estimations corresponding to vessel segmentation results in Fig. 3.3. The black pixel denotes no vessel is detected and the retinal vessel shadow is removed. 33

3.6 Active deformable surface models. (a) 10 $\times$ 10 control points. (b) An example of deformable surface obtained by 2D interpolation to control point array. 34

3.7 (a) $\sim$ (c) are top, side, and Bird's-eye views of a volume rendering images of choroidal vasculature. (d) Choroidal vasculature thickness map. 35

3.8 Plots of choroidal vessel diameter versus depth from the RPE in two subjects. Box and whisker plots (a)(c) and standard deviation plot (b)(d) exhibit the distribution of choroidal vessel diameter at a specified depth from the RPE. The red curves show the mean of choroidal vessel diameter. 36

3.9 Comparison of ICGA (a), *en-face* projection of vessel diameter volume (b), and depth-resolved *en-face* projection of vessel diameter volume (c) of 6 mm $\times$ 6 mm macular region obtained from the same subject. 37

3.10 Choroidal thickness maps obtained in 8 eyes of 4 healthy volunteers. The maps in a same row were acquired from the two eyes of a single subject. OS/OD: Oculus dexter/sinister; N: Nasal; T: Temporal; S: Superior; I: inferior. Black dashed line in left image in the third row denoted the position of B-scan shown in 3.11. 39

3.11 A B-scan image extracted from OCT volume corresponding to left image in the third row in 3.10. 40

3.12 Depth-resolved projections of vessel diameter volume corresponding to the choroidal thickness maps in 3.10. 41

A.1 The optical scheme for the caricaturization of a resonant EOM. 48
A.2 Experimentally obtained relationship between the modulation depth (A_0) and the driving amplitude (V). 51

B.1 Comparison of the measured phase retardation distribution with different $ESNR$ in the simulation and experiment. The sample is an eighth-waveplate in (a)-(d) and a quarter-waveplate in (e)-(h). (a),(c),(e), and (g) show the results of numerical simulation and (b),(d),(f), and (h) are the experimental results. The marked $ESNR$ values denote the mean $ESNR$ in each experiment or simulation. 57
B.2 Skewness of the distribution of phase retardation (δ_M) obtained by Monte-Carlo simulation for several true phase retardations. 58
B.3 Estimations of several set true phase retardations using 2^{16} trials of the measured phase retardation. The red and green solidlines denote the estimation results using mean and 4th order MCB estimators, respectively. The black dashed lines denote the true values. 58
B.4 Contour plots of systematic error in mean estimator (a) and 4th order MCB estimator (b). 61
B.5 Simulated precision of mean and MCB estimator for 2^{16} trials. The red, green, and blue curves represent the mean error energy corresponding to a mean estimator, 4th order MCB estimator, and 6th order MCB estimator, respectively. . . 61
B.6 Contour plots of RMSE in mean (a), 4th order MCB (b), and 6th order MCB estimator (c). 62
B.7 Estimation result in simulation and experiment. The true values are denoted by black dashed lines, and the mean and MCB estimation results are denoted by red and green lines, respectively. The solid lines denote the mean of a 65536-trial estimation, and the squares, circles, and crosses denote 64-measurement estimations of a quarter wave-plate, one eighth wave-plate, and glass in the experiment. 63
B.8 B-scan images of *in vitro* chicken breast muscle. (a) is an intensity image, and (b) is a log-scaled $ESNR$ image. (c) is a single raw phase retardation image. (d) and (e) are phase retardation images obtained from mean and MCB estimators based on 128 B-scans. The white dashed lines denote the positions of the depth signal shown in Fig. B.9 65
B.9 Plots of A-line signals versus penetration depth. The red dots represent phase retardation values of raw phase retardation (a), obtained by mean estimator (b), and obtained by 4th order MCB estimator (c). Dashed curves represents corresponding ESNR values. The ESNR of (a) is a raw and non-averaged ESNR signal, while the ESNR of (b) and (c) are averaged ESNR of A-lines which have been taken at the same location on the sample and been utilized for the estimation. 66

List of Tables

2.1 Properties of several ocular layers in PS-OCT images 9

Abstract of dissertation

The choroid is an internal layer of the eye with several basilic functions including the blood supply to the retina pigment epithelium (RPE) and the inner retina. Imaging the choroidal is critical to diagnose several ocular diseases associated with blood circulation. However, the choroid defies most of high resolution biomedical imaging methods because of it is anatomically deep from the optical visible surface of human body. Optical coherence tomography (OCT) has been a revolutionized imaging method in ophthalmology for its non-invasive feature, high resolution, and cross-sectional/three-dimensional imaging ability. While a large number of state-of-the-art imaging processing methods have been developed to process retinal OCT, algorithms for choroidal OCT are not as well developed because of penetration issue in conventional OCT systems at 800-nm wavelength.

OCT system with wavelength band of 1060 nm provides enhanced penetration to the choroid. Valuable biomedical information can be obtain by analysing the choroidal OCT data. In this dissertation, two procedures have been developed to investigate the choroidal properties in high-penetration OCT data.

The choroidal thickness is an parameter drawing much interest in ophthalmology. It is mainly measured by manual segmentation method, which is time-consuming and lack of histological evidence to validate the real chorio-scleral interface. Polarization-sensitive (PS-) OCT with 1-μm probe is suitable to segment the choroid since there is significant difference between birefringence properties in the choroid and sclera. The real chorio-scleral interface can be visualized in phase retardation tomographies provided by PS-OCT. A full automatic choroidal thickness measurement algorithm has been developed based on intensity and phase retardation contrast obtained.

Alternation of the choroidal vasculature is considered to be related to several ocular diseases such as aged-related macular degeneration and glaucoma. Visualization and quantitative analysis of the choroidal vessel may play an important roll in investigation of those circulation-related diseases. A choroidal vessel characterization framework is developed to analyse the volumetric choroidal OCT data. The choroidal vessel is segmented by a customized multi-scale adaptive thresholding method, and then the its diameter is estimated using morphological analysis. The entire thickness of the choroidal vasculature is also measured in the reconstructed choroidal vasculature volume.

Chapter 1

Introduction

1.1 Background

Optical coherence tomography (OCT) provides high-resolution depth-resolved images of biological tissues noninvasively [1], hence, it is very suitable for applications in ophthalmology. OCT has been a common clinical imaging method to examine the retina and choroid [2–5], which are anatomically deep from the body surface and challenge most of other high resolution biomedical imaging methods. The OCT technique has dramatically improved in terms of imaging speed, sensitivity, and resolution in the past two decade since its invention [6–10]. All of those technical promotion have significantly contributed to the utility of OCT in ophthalmic investigation and clinical application.

As popularization of OCT application, the amount of imaging data available to ophthalmologists also is dramatically increasing. To release tense manual work requirement, a variety of successful algorithms for computer-aided diagnosis by means of OCT image analysis are presented accompanying with system development and promotion [11]. Especially, automated analysis of OCT data effectively ease or improve clinical decision. Image processing is one of the major parts of computer-aided analysis in OCT application. It enhances structural or functional OCT images or segments some specific objects from them, providing essential information for further visualization or analysis of OCT data. Hence, OCT image processing is critical for recognition regions or tissues of interest or delineation features with clinical values. Currently, most of the image processing algorithms for ophthalmic OCT are specialized for retina imaging. The customized algorithms have achieved image enhancement, sub-layer segmentation, as well as some other functions with amazing performance reported literatures. Those excellent algorithms are essential factor that contributes to the booming of retina research in recent several years.

The choroid is an internal layer of the eye lying between the retina and sclera. It accounts for most of the ocular blood flow, providing metabolic support to the retinal pigment epithelium (RPE) as well as the inner retina. It is considered that the morphological variation indicates circulation abnormality related to several common ocular diseases such as aged-related macular degeneration (AMD) and glaucoma. Imaging and quantitatively evaluation of the choroid is of significant interest in ophthalmology. However, the choroid defies several conventional optical imaging methods, including OCT with a 800-nm wavelength band, because of the strong light scattering and absorption characteristics of the RPE.

1 μm wavelength band light, located in a local minimum of water absorption, has also been utilized by OCT to image the posterior segment of the eye [12–14]. Utility of 1-μm probe offers an enhanced penetration to the choroid. Volumetric data can be obtained in the deep layers in the posterior segment of the eye including the entire choroid and some part of the sclera. All of referred data was acquired by OCT systems with 1-μm wavelength probe unless otherwise specified.

1.2 Aims of thesis

The general aim of the works described in this dissertation was to develop several algorithms for automatic and effective analysis of choroidal OCT data. There were two specific topics contributing to the general aim: the first topic described a automated algorithm to measure the entire thickness of the choroid by PS-OCT; the second topic proposed a framework to characterization and enhanced visualization of the choroidal vessel in structural OCT volume. This two topics focused on either the macroscopical or microscopical information of the choroid, providing detailed parameters representing broad description of its status *in vivo*.

1.3 Thesis overview

This thesis is divided into 4 chapters. An overview of each of the remaining chapters is as follow:

- Chapter 2 presents an automated choroidal thickness measurement method by PS-OCT in detail. The anterior and posterior boundaries of the choroid are segmented based on intensity and phase retardation contrasts provided by PS-OCT simultaneous. The performance of this algorithm is evaluated in PS-OCT images acquired from *in vivo* macular region.

- Chapter 3 proposes a framework to analyse the choroidal vessel information. A customized multi-scale adaptive thresholding method is developed to segment the choroidal vessel in *en-face* slices extracted from a OCT volume. Then, the choroidal vessel thickness and the entire choroidal vasculature thickness are measured by a morphological operation based analysis and a deformable surface model. The reconstructed 3D choroidal vasculature and depth-resolved vessel projection offer both enhanced visualization and quantitative characterization of the choroid.

- Chapter 4 provides some concluding remarks of this dissertation.

In addition, appendix **??** describes an EOM calibration method for EOM based PS-OCT, and appendix B introduces a Monte-Carlo-based phase retardation estimator for systematic error cancellation in phase retardation measurement by PS-OCT.

Chapter 2

Choroidal thickness measurement by PS-OCT

Abstract

In this chapter, an automated choroidal thickness measurement algorithm is presented based on polarization sensitive optical coherence tomography (PS-OCT). The superficial and inner boundaries are automatically detected in intensity tomography and phase retardation tomography, respectively. The superficial boundary, RPE/choroid interface, is segmented by searching the local maximum derivative of the intensity in region just beneath the RPE. A phase retardation oriented chorio-scleral interface (CSI) segmentation approach is also developed to determine the posterior interface of the choroid. This approach employs a two-step scheme based on the phase retardation variation detected by PS-OCT. In the first step, a rough CSI segmentation is implemented to distinguish the choroid and sclera by using depth-oriented second derivative of the phase retardation. Second, the CSI is further finely defined as the intersection of lines fitted to the phase retardation in the choroid and sclera. This algorithm challenges the current approaches in which the CSI is determined by back-scattering contrast, which do not represent the real CSI based on anatomical and morphological evidence. The proposed algorithm provides a rational segmentation method for the morphological investigation of the choroid. Applications of this algorithm are demonstrated on *in vivo* posterior images acquired by a PS-OCT system with 1-μm probe.

2.1 Introduction

The choroid is an internal layer of the eye with several basilic functions. It accounts for most of the ocular blood flow [15], providing metabolic support to the retinal pigment epithelium (RPE) and the inner retina [16]. The choroid also plays a roll in the absorption of excess light penetrating the retina and the RPE and stabilizing the temperature of the macula [17]. Its thickness is related to several ocular pathological parameters, e.g., the intraocular pressure, perfusion pressure [18], and endogenous nitric oxide production [19]. The morphological investigation of the choroid is of significant interest in the diagnosis and study of ocular diseases such as glaucoma [20] and age-related macular degeneration [21]. However, the choroid defies the conventional optical imaging methods because of the strong light scattering and absorption characteristics of the RPE. Indocyanine green angiography (ICGA) [22–24], which relies on near-infrared wavelength, allows visualization of choroidal vessels, but it does not provide depth-resolved information. Ultrasonography is another approach used for choroidal examination [25], but its resolution is limited by a trade-off between detection depth and resolution.

OCT has been a common imaging method in ophthalmology [2, 26, 27]. The OCT technique has been dramatically improved in terms of imaging speed and resolution in the past two decades since its invention [28, 29]. The branch of Fourier-domain OCT (FD-OCT), including spectral-domain OCT and swept-source OCT, provides up to 20MHz scanning speed [28, 30], as well as enhanced sensitivity and signal to noise ratio (SNR) [6, 7, 31]. The increased acquisition speed to time domain OCT (TD-OCT) allows repeated 2D imaging of the retina, providing the possibility of speckle reduction and SNR improvement by averaging OCT images. Recently, the enhanced depth imaging (EDI) OCT technique has been developed and utilized to study the cross-sectional structure and measure the thickness of the choroid [32, 33]. Another approach to obtaining a choroid image using OCT, the application of a 1-μm wavelength probe, is rapidly being developed for its high penetration ability in the posterior segment of the eye [13, 34–37].

Most retinal segmentation algorithms are achieved by using back-scattering intensity information obtained by conventional OCT [11]. This intensity based segmentation relies on image contrast properties of each retinal layer, which have been widely investigated by comparing OCT images and histological studies. Various methods have been developed for the robust and fully automated segmentation of retinal OCT images. Hee et al. proposed the first segmentation method in TD-OCT based on intensity variation [38]. Since then, various methods have been developed for the segmentation of OCT images. Recently reported automated segmentation can provide robust segmentation of several sub-layers in the retina with superior precision to manual segmentation [39, 40]. However, when it comes to the choroid, there is a lack of morphologic knowledge. Its thickness would become significantly reduced when cut off from its blood supply. This makes it difficult to acquire knowledge of the chorio-scleral interface (CSI) in morphology *in vitro*, and hence it has been impossible to define the CSI in an OCT image based on histological knowledge. Most of the current OCT studies about choroidal morphology are based on manual segmentation. Ophthalmologists manually and empirically identify CSI. How-

Table 2.1: Properties of several ocular layers in PS-OCT images

	Intensity properties	Phase retardation properties
RPE	Hyper-reflective	Scrambling or preserving
Choroid	Randomly distributed	Preserving
Sclera	Homogeneous	Increasing as penetration depth

ever, to the best of our knowledge, no clear morphological or anatomical evidence supports the empirical manual segmentation of CSI. Recently, Kajić et al. reported an automated choroidal segmentation approach using a statistical model [41], but the training data for the construction of this model was still obtained by manual segmentation of intensity OCT images.

Polarization sensitive OCT (PS-OCT) is a functional extension of OCT providing intensity tomography and birefringence tomography simultaneously [42–45]. Tissues consisting of organized microstructure or collagen alter the polarization status of light, reflected as a phase retardation change or other birefringent parameters. Several studies have reported retinal imaging using PS-OCT. The phase retardation and birefringence of the retinal nerve fiber layer has been well investigated [46,47]. Götzinger et al. reported a functional segmentation of RPE using depolarization information obtained by PS-OCT [48].

Birefringent properties of the choroid and sclera have a clear difference [46]. The sclera represents a strong birefringence because of its high concentration of of collagen, and hence the phase retardation should increase along the penetration. Meanwhile, despite of a small amount of collagenic components in the choroid, the choroidal birefringence is so low that it is negligible for the PS-OCT system with a typical birefringence sensitivity. And hence the phase retardation can be reasonably considered as constant in the choroid [49]. This has been validated by high penetration PS-OCT using a 1-μm probe reported by Yamanari, et al. [50]. The depth-resolved birefringence properties measured by PS-OCT can be utilized as a contrast source for the segmentation of these tissues.

In this chapter, An automated segmentation algorithm is introduced to measure the thickness of the choroid based on intensity tomography and phase retardation tomography simultaneously obtained by PS-OCT. The boundary between the RPE and the choroid is segmented based on the high intensity gradient in intensity images. The CSI segmentation approach consists of two steps: Firstly, a rough segmentation is achieved by model analysis and a dynamic programming algorithm in the phase retardation image to initialize further respective phase retardation analysis in choroid and sclera. Next, linear regressions are applied to both layers near the rough segmentation results, and the CSI is determined by the intersection of the two fitted lines. Finally, a back-scattering based error detection and correction algorithm is performed to avoid the segmentation error caused by large vessels. Several results of this algorithm are presented to verify it efficiency in automatical choroidal thickness measurement.

2.2 Image acquisition and enhancement

In this study, a full-range Jones matrix PS-OCT system with a 1-μm probe beam has been employed for the polarization sensitive measurement [50]. The principle and setup of the Jones matrix PS-OCT has been reported in detail elsewhere [50–52]. In this system, the Jones matrix detection is achieved by modulating the incident light using an electro-optic modulator (EOM). It creates modulation-multiplexed two orthogonal polarization states. This polarization modulation results in two multiplexed OCT spectra with different carrier frequencies, i.e., a null-frequency and the same frequency with the polarization modulation. Both of the multiplexed spectra are then detected by polarization diversity detectors consisting of horizontal and vertical detectors. The OCT signals corresponding to the two carrier frequencies are numerically demultiplexed after detection. Since the OCT signals are multiplexed both by the carrier frequency and the polarization diversity detection, I finally obtain 4 OCT signals simultaneously. And then the cumulative Jones matrices of a sample are obtained by assigning the 4 OCT signals to each element of the Jones matrices. High-penetration Jones matrix tomography can be obtained from the posterior segment of eye by this PS-OCT system, and successive signal processing provides the corresponding phase retardation tomography.

Image quality is critical for biomedical image segmentation, especially for computer-assisted segmentation tasks. Speckle noise and a limited SNR are two of the main issues resulting in difficulty with segmentation. As reported in recent research, the signal to noise issue introduces both systematic and random errors in phase retardation measurement in the Jones matrix PS-OCT [53]. Usually, the SNR of an optical signal back-scattered from the CSI is low. It results in randomness and a low contrast in phase retardation tomography. This prevents an accurate quantitative analysis of phase retardation, leading to the failure of phase retardation information based CSI segmentation. To improve the quality of the phase retardation images, I measured several B-scans repeatedly in a same position of the eye, and performed the Jones matrices averaging described in [54].

Figure 2.1 shows intensity and phase retardation images resolved from a single Jones matrix B-scan and averaged Jones matrix B-scan. Figure 2.1(c) reveals that the averaging strongly reduced the speckle noise in intensity image and improves the SNR. It is also shown in Fig. 2.1(d) that an enhanced phase retardation contrast appears around the CSI.

2.3 RPE/choroidal interface segmentation based on intensity contrast

The RPE is known as the most inner layer in the hyper-reflective complex in a OCT image acquired in the posterior segment of the eye. It appears as a high intensity image strip above the choroid, while the choroid has a lower intensity signal than the RPE complex. Hence, the local maximum gradient represents the interface between the RPE and the choroid in an intensity OCT

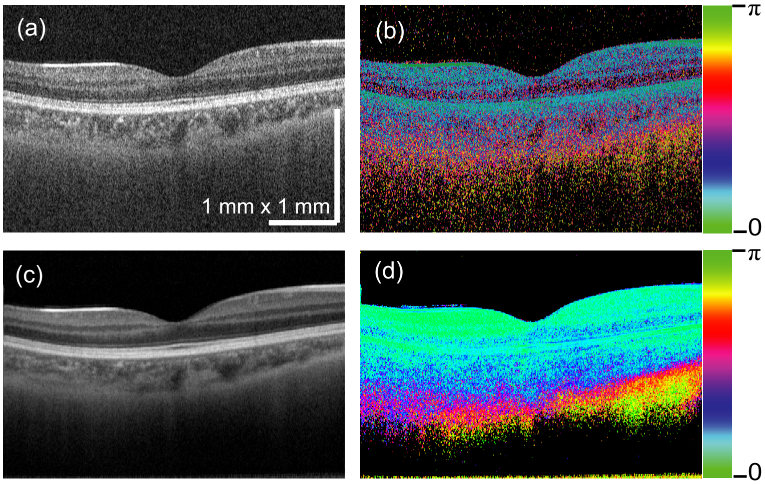

Figure 2.1: The efficiency of the Jones matrix averaging of 16 B-scans. (a) and (b) are the intensity image and phase retardation image extracted from single B-scan in PS-OCT, respectively. (c) and (d) are the intensity image and phase retardation image extracted from the average of 16 Jones matrix B-scans, respectively.

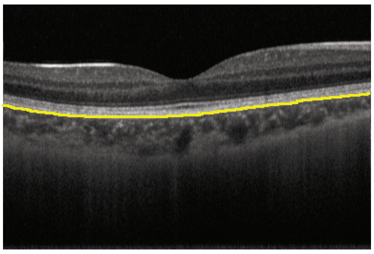

Figure 2.2: Segmentation of the RPE/choroid interface.

image. Segmentation of this layer has achieved by different methods such as pixel clustering [40], dynamic programming [39, 55], and active contour [56, 57].

Here the algorithm firstly adopts a similar method as 58 for RPE estimation. This estimation detects the RPE by searching the pixels with the maximum intensity value in each A-lines. Because the shadow signal of the retinal vessel or non-edge region can degrade the segmentation result, a Savitzy-Golay filter is performed to smooth the segmentation result. A smooth line denotes the RPE position is detected after an additional median filter. Then, the interface of the choroid and RPE is assigned to the pixels with minimum negative gradients beneath the RPE estimation in the intensity OCT image blurred by using a Gaussian filter with a standard deviation of 3 × 3 pixels. The yellow line in figure 2.2 indicates the RPE/choroid boundary segmented using this method.

2.4 Two-step CSI segmentation based on phase retardation contrast

Since the sclera is a collagenous tissue and the choroid is not, the birefringence properties in choroid and sclera are quite different. In this work, the CSI is determined as the boundary between areas with different phase retardation properties. The gradient of phase retardation is used to represent the birefringence. The segmentation approach consists of two steps. A rough segmentation is implemented in advance for the initialization of subsequent phase retardation analysis. Then, depth-oriented linear regressions are applied to the phase retardations in both the roughly segmented choroid and the sclera for an exact segmentation.

2.4.1 Rough segmentation

The second step of our algorithm is based on the depth-oriented slope fitting of the phase retardation which is applied to the choroid and sclera separately. Therefore, the interface of these layers should be roughly identified in advance. The purpose of the rough segmentation from the first step is to determine the ranges of linear regressions for the second-step of our algorithm.

Since the amount of birefringence is low in the retina and choroid, I model the phase retardation in the choroid as a small constant value, i.e., a linear line with a slope of zero in depth. On the other hand, sclera has a strong birefringence, and hence I model the scleral birefringence as a linear line with a positive slope in depth. In this model, the CSI is detected as a local maximum of the second derivative of the phase retardation in depth. In our implementation the second derivative is obtained by a discrete operator of [-1 0 0 0 0 2 0 0 0 0 -1], which is equivalent to a wide kernel first derivative operator of [-1 -1 -1 -1 -1 1 1 1 1 1] and the successive standard first derivative operator of [-1 1]. The wide kernel operator is used to enhance the derivative value and improve the SNR of the second derivative. This second derivative possesses a local maximum at the CSI, while minor fluctuations of the phase retardation are filtered out. The location of the local maximum is utilized as the first estimation of the CSI in the next procedure.

In this implementation, The speckle noise is firstly reduced using a rectangular averaging filter (size: 30 × 10 pix = 100 μm (lateral) × 79 μm (axial)) in the phase retardation images. This moving average significantly reduces the speckle in a phase retardation image as shown in Fig. 2.3(a). Then, the second derivative of the despeckled phase retardation was obtained along penetration in each A-line using the protocol described above. The distribution of the second derivative is shown in Fig. 2.3(b). A local maximum band can be observed around the expected CSI.

However, in Fig. 2.3(b), the CSI is not the only layer detected as local maximum. The strongest signal appears around the inner limiting membrane. Region of interest, the choroidal and scleral areas, are selected based on the RPE/choroid interface segmentation achieved by the method described in Sec. 2.3. Then, this boundary is shifted 5 pixels (40 μm) towards the choroidal side to exclude the RPE from the region of interest. All of the pixels anterior to the choroid/RPE interface as well as other pixels with a negative second derivative value or an

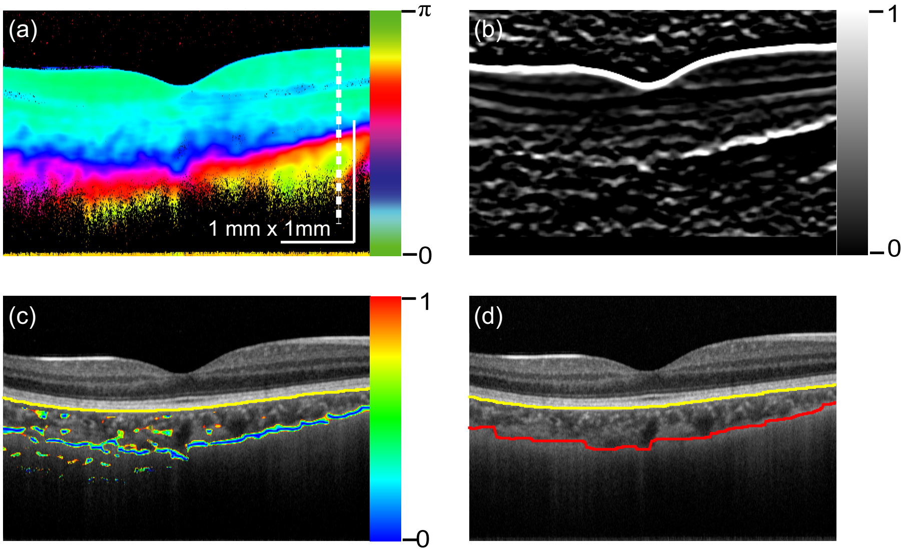

Figure 2.3: Illustration of rough segmentation flow. (a) Speckle reduced phase retardation image. (b) Distribution of second derivative in the B-scan image. (c) The node cost distribution of potential CSI are masked on the intensity OCT image. The yellow line shows the segmented RPE/choroid interface. (d) Rough segmentation result is shown in red.

intensity lower than twice of noise floor are set to 0. Then, the second derivative information is normalized in each A-line. Here $d(i, j)$ are used to denote the normalized second derivative of the j-th pixel in the i-th A-line. Figure 2.2 shows an example of RPE/choroid interface segmentation result.

To obtain a continuous curve as the CSI estimation, a graph searching method are applied using dynamic programming based on the second derivative information. The dynamic programming method has been used in several automated segmentations of retinal layers in intensity OCT images, providing a robust solution to shortest path or minimum cost problems without an initialization of start and end points [39, 55, 59]. To apply the graph searching method, All pixels are firstly classified into either a potential CSI or a false CSI. The pixels meeting the condition of d(i, j) $\geq$ 0.5 are classified as potential CSI and the others are classified as false CSI. Furthermore, the node costs of these two types of pixels are assigned as

$$c(i,j) = \begin{cases} 2 & for\ d(i,j) < 0.5 \\ 1 - d(i,j) & for\ d(i,j) \geq 0.5 \end{cases}. \tag{2.1}$$

The node cost of potential CSI slope is shown in Fig. 2.3(c) with a rainbow color-map superimposed on an intensity image, where transparent is assigned to the node cost of 2. In this definition, the node cost at a potential CSI ranges from 0 to 1, lower than half of the node cost in a false slope position. This setting can effectively limit the segmented CSI within the potential CSI

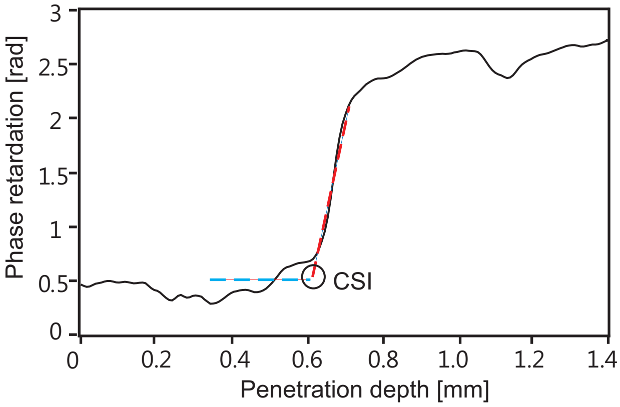

Figure 2.4: Illustration of the slope fitting model in phase retardation. The black curve shows the phase retardation A-line signal marked with a white dashed line in Fig. 2.3(a) The blue and red dashed lines are the linear regression lines of phase retardation in the choroid and sclera, respectively. The CSI is determined by the intersection of these two lines.

band, isolating it from the fake patches of local maximum in the second derivative distribution.

The minimum cost from the first A-line to node (i, j) in this dynamic programming algorithm is represented as

$$cost(i,j) = \begin{cases} c(i,j) & i = 0, 0 \leq j < M \\ \min\limits_{j-1 \leq n \leq j+1} cost(i-1,n) + \sqrt{|n-j|+1} c(i,j) & 0 < i < N, 0 \leq j < M \\ \infty & other\ cases \end{cases}, \tag{2.2}$$

where M and N are the number of pixels in an A-line and the number of A-lines in a B-scan, respectively. $\sqrt{|n-j|+1}$ in the second case is a distance parameter that reflects the distance penalty in the graphic solution.

The optimal solution is defined by searching the path with minimum cost from the leftmost A-line to the rightmost A-line. A 50-pixel (3.3% of the transversal range) median filter is also applied to reject minor segmentation error. This solution is shown with a red line in Fig. 2.3(d).

2.4.2 Slope fitting in phase retardation

The gradient of phase retardation reveals birefringence properties in the tissue. Phase retardation increases rapidly with penetration in the sclera due to the presence of birefringent components, while remaining almost a constant in the choroid. The boundary of these two layers should appear as an inflection in the phase retardation model. The exact segmentation to the CSI is achieved by slopes fitting to cumulative phase retardation in the choroid and sclera as described in following paragraphs.

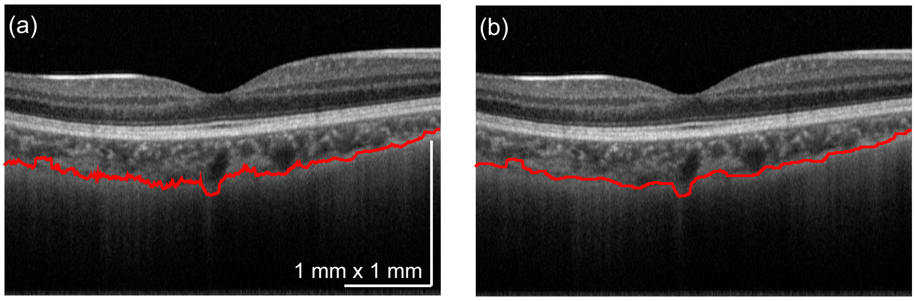

Figure 2.5: The CSI obtained by fitting the phase retardation model shown in Fig. 2.4(a). The red curve shows the intersections of the linear regression lines in each A-scan, (b) The CSI smoothed by a median filter.

The phase retardation model in the choroid and sclera is illustrated in Fig. 2.4. Constant phase retardation in the choroid is assumed in this model. An average of the phase retardation is obtained between the RPE/choroid boundary and the initial estimation of the CSI for each A-line, where the RPE/choroid boundary was segmented by using the intensity image as described before, and the initial estimation of the CSI was obtained by the method described in 2.4.1. This averaging is equivalent to a linear regression to the phase retardation in the choroid by a regression line with zero. Linear regressions are applied to the 7-pixel (55-μm) regions in the sclera close to the initial estimation of the CSI. Since the initial segmentation might lack accuracy, I do 11 trials with the start point of this linear regression from -5 pixels to +5 pixels (-40 μm to +40 μm) to the initially estimated CSI, and select the regression with the maximum gradient as the phase retardation slope in the sclera. This operation is for excluding the choroidal and scleral regions with aliasing of the phase retardation from the linear regression since these two regions have low phase retardation that minimize the gradient. The CSI of each A-line is defined as the intersection of these two lines as shown in Fig. 2.4(a). Finally, the CSI is acquired by smoothing the intersections in the B-scan direction by a 50-pixel median filter.

2.4.3 Error correction

A large blood vessel in the choroid or sclera can disturb this phase retardation information based CSI detection. The anterior boundary of a blood vessel is sometimes detected as the CSI by this algorithm. One reason might be the unreliable measurement of the phase retardation in the blood vessels. The back scattering signal from blood is very weak, so the SNR inside of a blood vessel is relevantly low. As it was revealed in Ref. 53, measured phase retardation would approach around 2/3 π as the effective SNR decreases. This erroneous high phase retardation would mimic the phase retardation in the sclera. The collagen in the vessel wall can also be a factor that misleads our phase retardation oriented CSI segmentation.

To eliminate the segmentation error around a large vein, an additional optimization algorithm

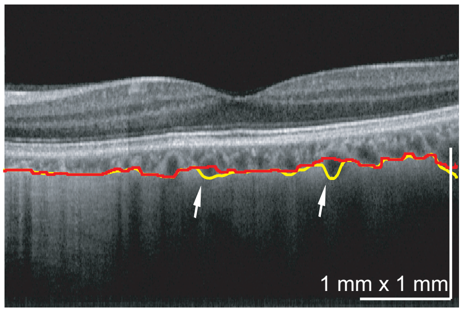

Figure 2.6: An example of intensity based segmentation error correction. The red and yellow lines denote the phase retardation based segmentation of the CSI and the intensity based correction result.

based on an intensity image is applied. Identification of blood vessel's position around the CSI is required in error correction. This is achieved by the analysis of intensity information beneath the CSI obtained in the two-step segmentation process described in Section 2.4. The intensity inside the blood is rather weak due to the low back scattering from blood. A moderate intensity can be observed in the sclera near the CSI, and the intensity constantly decreases along penetration in the intensity images acquired by PS-OCT. Note that this feature is only warranted in polarization-independent intensity OCT images, which are free from the birefringence artifact that exists in standard OCT images [13, 60]. We distinguish the segmentation error by evaluating the distance between the segmented CSI and the pixel with maximum intensity beneath it in each A-line. If this distance is higher than a threshold, e.g. 5 pixels, the CSI would be corrected to the maximum intensity position, which indicates the posterior boundary of a blood vessel. In the end, a median filter with the width of 25 A-lines is utilized to reject the false correction that can happen in a single A-line.

Fig. 2.6 shows an example of an intensity based segmentation error correction. As indicated by white arrows, the phase retardation based segmentation result is located within blood vessels in some regions. It is clear that the phase retardation failed in segmentation of the CSI. These errors can be detected and corrected by the intensity based process described above. The corrected segmentation result shown with a yellow line in Fig. 2.6 provides a more reasonable estimation of the CSI around the vessel regions.

2.5 Results

2.5.1 Performance of the CSI segmentation by PS-OCT

An 1-μm probe polarization sensitive swept source OCT was utilized to obtain phase retardation and back-scattering images. The setup and parameters of this system have been described in Ref. 50 in detail. *In vivo* multiple B-scan imaging has been performed in healthy eyes. The macular

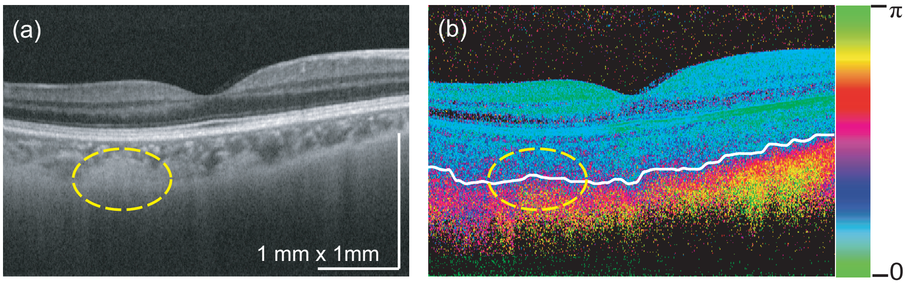

Figure 2.7: PS-OCT images of the macular region. (a) Intensity image, (b) Phase retardation image. The white line in (b) shows the CSI segmentation by phase retardation based segmentation.

region of the retina is imaged with 1,500 A-lines per frame and 64 frames are repeatedly acquired in a 5-mm horizontal area centered at the fovea. The probe power on the cornea was 0.81 mW.

The axial motion was detected and canceled by a custom-made correlation based algorithm. In this algorithm, a B-scan frame is selected as a reference. The cross-correlation functions between an A-line in the reference frame and the A-lines in the corresponding transversal location in the other frames are calculated. These correlation functions provide the axial displacement of each A-line respect to the reference frame. The outliers in the detected displacement within a frame were eliminated by applying medial filtering with a kernel size of 100 A-lines. The intra-frame-motion respect to the reference frame was then corrected by using the predicted displacement for each frame. After this motion correction, the image correlations between the reference frame and all of the motion corrected frames were calculated, and the most highly correlated 15 frames were selected. An averaged Jones matrix B-scan was yielded from the 15 frames and the reference frame by using the Jones matrix averaging algorithm [54].

Six subjects without marked posterior disorder were involved in this study. Six eyes of three subjects were first measured. A high similarity between the two eyes of the same subject was observed. Hence, only one eye from each remaining subject was scanned. Finally, six eyes of the six subjects were involved in the following study.

An example of phase retardation based segmentation is shown in Fig. 2.7. This B-scan is acquired from a myopic eye of an adult subject. In the region indicated with an ellipse in Fig. 2.7(a), the tissue appears as a homogeneous intensity feature. No structrural information indicates the location of the CSI, so it is difficult to determine whether the CSI is smooth or abruptly convex in this region. In the same region in Fig. 2.7(b), a clear difference in birefringence property can be visualized through phase retardation information. The real CSI can be detected as shown in Fig. 2.7 using the 2-step algorithm described in Section 2.4. The phase retardation based method provides more reliable CSI segmentation than the intensity based method.

In several previous studies about choroidal thickness, the choroidal thickness was manually determined at only a few representative locations, and the distribution of choroidal thickness is evaluated based on the thickness at these locations [61,62]. This method is based on the assump-

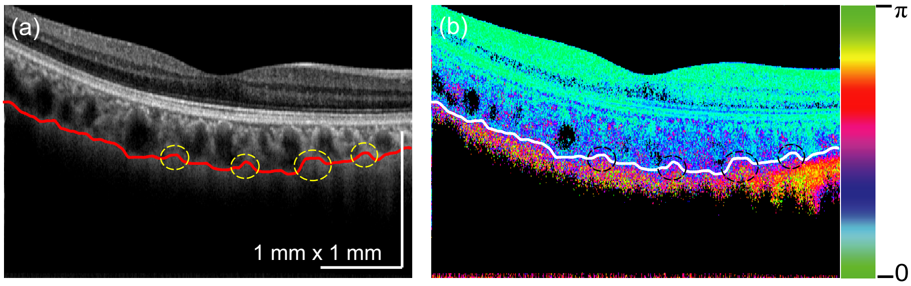

Figure 2.8: A phase retardation based segmentation result is shown in intensity image (a) and phase retardation image (b). The yellow and black ellipses marked several unsmooth segments in the CSI.

tion that the CSI is smooth. However, the phase retardation based segmentation results challenge this assumption. In Fig. 2.6, it is clear that the CSI appears to deviate around the large blood vessels in the thin choroid. Fig. 2.8 also gives an example of rough CSI. The CSI segments marked with yellow circles appear as convex patterns, contradicting the assumption of a smooth CSI. According to the phase retardation image shown in Fig. 2.8(b), the convex distributions of the phase retardation are also found in these regions, and the phase retardation based segmentation accurately represents them. This unsmooth CSI obtained by the phase retardation based segmentation was clearly observed in 3 out of 6 subjects.

Abnormal CSI segmentation associated with a low birefringence region beneath the fovea was sometimes obtained. Fig. 2.9 shows an example. It is clear that there is a region with abruptly low phase retardation around the CSI near the fovea. This phase retardation distribution was found in three out of six subjects, either with myopia or hyperopia. Since this CSI segmentation algorithm is based on the phase retardation information, the segmented CSI can be given as a concave shape. However, a corresponding concave structure cannot be found in the intensity image (Fig. 2.9(a)). One potential reason for this could be the alteration of the birefringence property in the sclera at the foveal region. However, neither the phase retardation nor the intensity information can provide indisputable evidence to identify the CSI. Further study including an in vitro histological study may be required to correctly understand this issue.

In measurements of one subject out of six, the penetration depth is quite limited in the choroid. The results are shown in Fig. 2.10. Both the intensity and phase retardation images are poor in the posterior choroidal region. Reasons for this might be a very thick choroid or strong light absorption. The low quality of phase retardation measurement leads to the failure of CSI segmentation. Even so, the algorithm still provided a reasonable CSI segmentation at the left part of the B-scan, i.e., at the nasal region. Further development and optimization of the PS-OCT hardware will provide higher signal intensity for these cases, and may solve this issue.

The repeatability of this method was also evaluated as follows. I first selected 16 B-scan frames from the 64 frames in a single dataset by the correlation based algorithm. An averaged

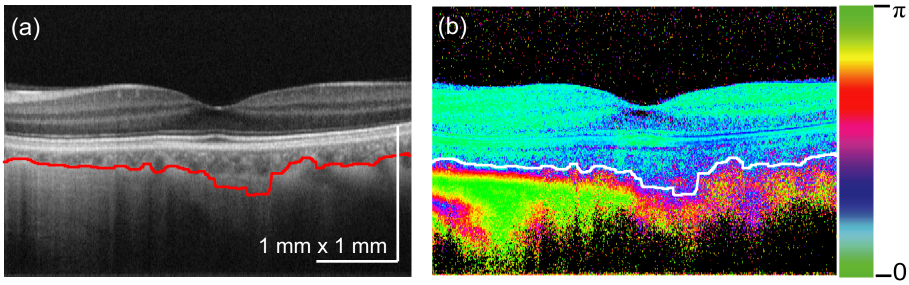

Figure 2.9: An example of segmentation in an eye with low birefringence in some scleral region. The red and white lines show the segmentation result in intensity image (a) and phase retardation image (b), respectively.

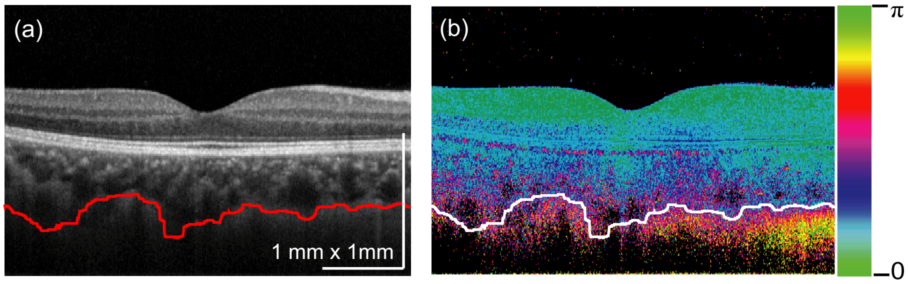

Figure 2.10: Intensity (a) and phase retardation (b) B-scans acquired from an eye with poor visualization of the posterior choroidal region. The CSI segmentation results, a red line in (a) and a white line in (b), cannot represent the real CSI.

Jones matrix image was created from these 16 frames. The RPE and the CSI were segmented from this averaged Jones matrix image, and the choroidal thickness distribution was defined as the distance between the RPE and the CSI. And then, another 16 frames were selected from the residual 48 frames by the same correlation algorithm, and the same operations including the averaging, segmentation, and calculation of choroidal thickness were performed. Namely, the segmentation was performed twice with two independent OCT images corresponding to the same location of the eye. Finally, the standard deviation of the difference of the choroidal thicknesses along the transversal direction was obtained. This standard deviation would provide a measure of repeatability of the segmentation algorithm.

2.5.2 Measurement of the choroidal thickness

I performed this evaluation with 4 datasets obtained from 4 subjects which show reasonable phase retardation distributions. The standard deviations of the difference of the choroidal thickness were 14.1 μm, 17.1 μm, 10.8 μm and 8.2 μm. These standard deviations correspond to 1- to 2-pixel depth of our PS-OCT image. And hence, the repeatability of our system is believed to be reasonable.

2.6 Discussion

In the Jones matrix PS-OCT, both the accuracy and precision of phase retardation measurement rely on effective SNR [53]. An effective SNR is mainly determined by the lowest SNR channels in the Jones matrix measurement. In our system, two of the four channels use a phase modulated probe beam achieved by an electro-optic modulator. The SNR in the modulated channels are more than 10-dB lower than that in non-modulated channels. Hence, the effective SNR level is limited to a relatively low range, raising both systematic and random error in the phase retardation measurement. This is one of the main issues that degrade phase retardation analysis and segmentation. We believe optimization of the PS-OCT system can promote segmentation accuracy and reduce the failure rate of the segmentation.

In this work, phase retardation image quality is enhanced by averaging several Jones matrix B-scans. Jones matrix averaging is very sensitive to eye motion among B-scans since the complex Jones matrix elements can counteract each other in the case of a mismatch. Transversal motion compensation is not implemented to save calculation time, only choosing a group of B-scans with less transversal eye motion from a set of B-scans. So there is a trade-off between noise reduction and signal preservation related to the number of B-scans in Jones matrix averaging. Increasing the B-scans number can reduce the noise level, but degrade the accuracy in phase retardation measurement. The optimal phase retardation image quality is limited by this trade-off. There are three possible solutions to this issue. An optimized PS-OCT system can acquire Jones matrix B-scans with high effective SNR, so fewer B-scans are required for noise reduction. Increasing the scanning speed can restrain the eye motion effect by shortening the acquisition time. A timesaving and effective motion compensation algorithm or extra motion tracking hardware [63, 64], might be able to further increase the averaged phase retardation image quality.

Although the choroid is a phase retardation preserving layer, a moderate increase in phase retardation was sometimes observed in the choroid along the depth. This could be because of a systematic error caused by the decreasing effective SNR. A Monte-Carlo-based phase retardation estimator can restrain systematic error introduced by noise [65]. However, this method requires an accurate effective SNR value for each pixel. The Jones matrix averaging is a complex averaging process. Although the Jones matrices have a non-correlated global phase to each other, the global-phase is cancelled before the complex averaging [54], a small amount of residual global phase results in an out-of-phase summation of the signals and degrades the effective SNR. Since this signal degradation is not fully predictable, the Monte-Carlo-based phase retardation estimator can not always provide a correct estimation of the phase retardation. Therefore, I did not apply the Monte-Carlo-Based estimator in this study. Further optimization of PS-OCT hardware will improve the sensitivity, and will eliminate the necessity of Jones matrix averaging. The Monte-Carlo-Based estimator could be a powerful aid to phase retardation based CSI segmentation for an improved future version of PS-OCT.

In current status, an image with 1,500 (lateral) × 300 (axial) pixels requires around 12 seconds for the pre-processing and 10 seconds for segmentation with an algorithm implementation written in LabVIEW (LabVIEW 2011 for 64-bit Windows 7) on Intel CORE i7 CPU Q720 at 1.60 GHz with 8-GB RAM. The pre-processing includes motion cancellation, Jones matrix averaging, and phase retardation calculation, and the time consumptions are nearly equally distributed in these three processes. Among the sub-processes in the segmentation process, the rough segmentation is the most time consuming process, it takes around 7 seconds. I expect to shorten the pre-processing time by taking the advantage of a graphics processing unit (GPU) in the future, since the pre-processing can be heavily parallelized according to its mathematical properties. Although I are currently using a multi-core CPU, the program has not been well parallelized. The segmentation speed can also be optimized by proper usage of multiple CUP cores.

2.7 Summary

This chapter has reported an algorithm for automated and functional measurement of the choroidal thickness based on intensity and phase retardation information obtained by PS-OCT. The interface between the RPE and the choroid is segmented by detection of the maximum gradient just beneath the RPE complex. The choroid and sclera were modeled by linear incremental phase retardation along the depth. Segmentation was achieved by a two-step algorithm based on a phase retardation image followed by fine correction based on the corresponding intensity image. The first step of the two-step algorithm used the second derivative of the phase retardation image and a graph-search algorithm, and provided an initial estimate of CSI for the second step. The second step defined the CSI based on the difference of the phase retardation slopes of the choroid and sclera. Phase retardation tomography represents the depth-resolved birefringence properties in the sample, offering functional information above structure to recognize tissues. The phase retardation based CSI segmentation algorithm provides a reliable method for an investigation of CSI morphology. Associated with the segmentation of RPE/choroid interface, the ”real” choroidal thickness can be achieved with high accuracy. Currently, the number of subjects examined is six. Further study with a larger number of subjects and a larger variety of eyes including several refraction errors and several diseases would be important to strengthen the reliability of the algorithm.

Chapter 3

Enhanced visualization and characterization of the choroidal vessel by OCT

abstract

In this chapter, the research has been focused on the choroidal vessel. An automated choroidal vessel segmentation and evaluation algorithm is developed for advanced visualization and quantification of the choroidal vasculature by high penetration optical coherence tomography. The choroid is flattened to the retinal pigment epithelium and then choroidal vessel is segmented by a customized multi-scale adaptive thresholding method in *en-face* slices at each depth. Successively, the choroidal vessel thickness is evaluated by a series of morphological operations. Both structural and vessel thickness information are represented in a reconstructed 3D choroidal vasculature volume. Practicability of the proposed method is also validated by analysis of *in vivo* choroidal volume data acquired by optical coherence tomography system with 1-μm probe.

3.1 Introduction and background

As referred in Chap. 2, the choroid is a highly vascular layer lying between the retinal pigment epithelium (RPE) and the sclera in the posterior segment of eye, accounting for oxygen and nourishment supply to the outer layer of the retina [66, 67]. Chapter 2 measures the entire thickness of the choroid, but does not offer methods for investigation of the choroidal vessel. As reported, morphological alternation of the choroidal vasculature may play an important roll in some ocular diseases related to circulation abnormalities such glaucoma or aged-related macular degeneration (AMD) [68–70]. Hence, imaging of the choroidal vasculature draws significant interest in ophthalmology.

ICGA is currently an common method to image the choroidal vasculature in clinic [24]. However, ICGA only provide a *en-face* projection of dye contrast without depth resolution. Signal overlapping among different layers can degrade the vessel contrast especially in areas where the capillaries is dense. Moreover, ICGA requires dye injection, which is uncomfortable and can results in severe adverse reaction [71, 72]. Optical coherence tomography (OCT) has become a powerful imaging technique in ophthalmology for its cross-sectional or 3D imaging capability with high resolution [3, 5]. Currently clinical ophthalmic OCT systems employ a scanning light with 800-nm wavelength range, which can be significantly attenuated by the RPE because of strong absorption and scattering, providing a limited penetration into the choroid. Enhanced depth imaging OCT offers clear images in the choroid by adjusting the beam focus depth and averaging repeated B-scans [32]. This technique has been utilized to measure the choroidal thickness [32, 61]. But it is difficult for 3D visualization of the choroidal since the B-scan averaging limits its imaging speed. An alternative method that can access to the choroidal imaging by OCT is high penetration (HP-) OCT achieved by application of 1-μm probe wavelength [12, 13, 73]. Application of HP-OCT is rapidly developing for its capability of 3D choroidal imaging. It has been utilized in the choroidal thickness measurement [74, 75], the choroidal vessel network visualization [14], and non-invasive choroidal vessel angiography [76, 77].

The structure of the choroid is generally divided in to four layers: Haller's layer, Sattler's layer, Choriocapillaris, and Bruch's membrane from the outer to inner layers [67]. Besides the Bruch's membrane, the other 3 layers are formed by dense vessel and distinguished by their vessel diameters. Haller's layer consists of large diameter blood vessel, lying outmost layer of the choroid; Sattler's layer is a layer of medium diameter blood vessel; Choriocapillaris is immediately adjacent to Bruch's membrane with capillaries. The entire choroidal thickness has been regarded as an important parameter since it is highly related to several pathological effect in clinic or some other parameters [78, 79]. However, it does not fully represent the status of the choroid and can become invalid in diagnosis of some ocular diseases. E.g., it is reported that glaucoma can result in either thinning or thickening of the choroid in different stages [80]. A hypothesis considered it is caused by different interactions of the vasculature occurring in different sub-layers in the choroid [81]. 3D visualization and thickness measurement of the choroidal vessel can reveal detailed morphological variation of the choroid, offering a better understanding to the pathological phenomena. Hence, segmentation and parameter measurement of the choroidal vessel are critical for investigation and diagnosis of circulation-related diseases in ophthalmology.

Since vessel segmentation in medical image is an essential step of the diagnosis of various diseases, many state-of-the-art algorithms for vessel segmentation in 2D or 3D data have been proposed [82,83]. Choroidal vessel segmentation can provide not only a intuitive visualization of the choroidal vasculature but also an access to morphological information of the choroidal, which is important to understand pathogenesis of circulation-related ocular diseases. Generally, the vessel segmentation can be achieved by 2 types of strategies: region tracking from some given or detected seeds in vessels, or tracking-based methods; and extracting the boundary or ridge of the vessel using some filters, or window-based methods. Tracking-based methods are usually time-consuming, while window-based methods often require further refinement. Recently, Li et. al. developed an automated choroidal vasculature segmentation algorithm by using seeds detection and region growing approaches, providing 3D visualization and segmentation of the choroidal vasculature [84]. Kajić et. al. presented a fully automated vessel segmentation algorithm by employing multi-scale 3D edge filtering and projection of ”probability cones” to determine the vessel ”core” [85]. Though performing well in literatures, both segmentation algorithms are relatively complicate in mathematical model and programming. Adaptive thresholding is one of the most simplest window-based method of image segmentation. It generate a binary image from a gray-scale image by local threshold statistically examine by the neighborhood of each pixel. The backscattering coefficient of blood is much lower than that of other tissues, so the intensity of the OCT signal at vessel region is relatively lower than background. So adaptive thresholding method can be an simple candidate approach for choroidal vessel segmentation.

Quantitative analysis of choroidal vasculature plays an important roll in pathogenesis investigation and clinical diagnosis of several ocular diseases. Sohrab et. al. reported an method for quantitative analysis the choroidal vasculature in AMD patients using vessel density as a parameter in spectral OCT volumes, validating the potential of OCT in qualitative and quantitative choroidal vascularity evaluation [86]. However, the choroidal vessel features were not further evaluated in their work. The measurement of choroidal vessel thickness is the key of quantitative evaluation of choroidal vessel and discrimination of the internal layers in the choroid. The vessel diameter distribution can provide valuable information to understand the ocular blood supply condition. This task is challenged because the choroidal vessels are densely distributed and their orientations are highly zigzag.

In this chapter, I present an automated framework to segment and quantitatively characterize the choroidal vessel in volumetric OCT data obtained by HP-OCT. Firstly, the choroidal vessel is segmented by a customized multi-scale adaptive thresholding based segmentation algorithm in $en-face$ slices, which are aligned to the RPE, in each depth; successively, the thickness of choroidal vessel is measured by a serial of opening operations in morphology. The choroidal vasculature is shown in both 3D volume or depth-resolved *en-face* projection. The proposed approach can visualize the choroidal vasculature with vessel thickness information, providing a non-invasive quantitative analysis method for the choroidal vasculature investigation.

3.2 Choroidal volume extracting and flattening

The choroidal vascular pattern can be clearly visualized in the *en-face* slices extracted at different depth. A customized procedure is developed to segment the choroidal vasculature in *en-face* slices in the choroidal volume. Before the application of the segmentation algorithm, the choroid and a part of the sclera are segmented from the OCT volume and flattened to the RPE.

To identify the choroidal region and extract the choroid slices at each depth, the Bruch's membrane is segmented automatically. I employ a method similar to that utilized in [74] to segment the pixels with minimum negative gradients beneath the RPE in each B-scan. The segmentation result is approximately regarded as the Bruch's membrane, whose thickness is only several μm, similar with the pixel resolution of OCT system. 370-μm range beneath the Bruch's membrane is selected and flattened in the volume OCT data. Considering the typical maximum choroidal thickness around the macular, the selected volume covers all of the choroid and partial of the sclera in most cases. Local mean filter is performed to reduce speckle noise and enhance image quality in *en-face* slices at each depth. Figure 3.1 shows the despeckled slices extracted at difference depths in the choroid. The choroidal vessel network can be visualized with an increasing thickness as depth.

Beside the Bruch's membrane, the other boundary of the hyper-reflective complex, outer nuclear layer (ONL)/inner segment (IS) of photoreceptor layer, is also segmented by detect the maximum positive gradient above the RPE. The hyper-reflective complex is extracted from the volumetric data. The extraction of this layer is useful to recognize the shadow signal of the retinal vessel described in 3.3.3.

3.3 Multi-scale adaptive thresholding based vessel segmentation

3.3.1 Adaptive thresholding method

Adaptive thresholding method

Instead of local mean or local median approaches, robust automatic threshold selection [87], which is simple and fast in bi-level thresholding of grey-scale images, is utilized to find the local threshold in OCT slices since it is less sensitive to the ratio of vessel area in a local window. The

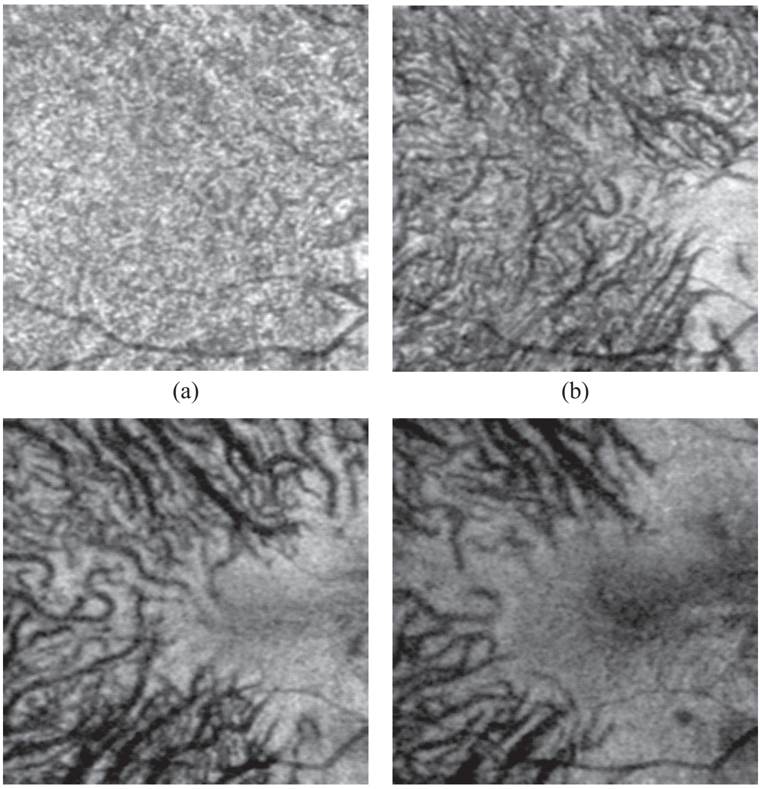

(a) (b) (c) (d)

Figure 3.1: *En-face* slices extracted at (a) 25μm, (b) 100μm, (c) 175μm, and (d) 250μm under the RPE in the OCT volume flattened to the Bruch's membrane.

local threshold is determined by

$$Threshold(x,y) = \frac{\sum\limits_{\substack{x-\frac{w}{2}<i<x+\frac{w}{2}\\ y-\frac{w}{2}<j<y+\frac{w}{2}}} I(i,j) * g(i,j)}{\sum\limits_{\substack{x-\frac{w}{2}<i<x+\frac{w}{2}\\ y-\frac{w}{2}<j<y+\frac{w}{2}}} g(i,j)}\ , \tag{3.1}$$

where $I(i, j)$ and $g(i, j)$ respectively represent the intensity and edge strength values at (i, j), which is a pixel locates in a window centered at pixel (x, y) with size of w. The edge strength is calculated as the root of summation of squared partial derivative of intensity in vertical and horizontal direction. The local threshold is calculated at all of the pixels in each *en-face* slice. If the pixel intensity is below the threshold it is set to vessel sign. otherwise it assumes the background value. In this paper, ”1” denotes vessel and ”0” denotes background in binary images.

Busyness filter

Figure 3.2 (b) is a binary image obtained by applying adaptive thresholding to fig. 3.2 (a) with a fixed moving window size. The main choroidal vessels can be segmented from the background. However, adaptive thresholding cannot properly distinguish background and vessel pixels if the local window including only background. It will generate artifact in vessel segmentation. E.g., some black pixels appear in the right middle area of fig. 3.2 (a), where is the sclera region without any vasculature pattern.

Normally, the vessel and background regions are quite distinct from each other in a binarized sub-image containing both vessels and the background. While the pixel intensity alternate frequently so that it seems that the ”vessel” pixels are more randomly distributed in a binarized sub-image containing only the background. Reasonably, edge busyness, which represents the jittery appearance of edges, are adopt as parameter to recognize and reject the artifact vessel pixels in non-vessel region [88].

I defined edge pixel as a pixel with binary value different with at least one of its 8 neighbor pixels in a binary image. The ratio of edge pixel in a local window is used to evaluate the busyness. Fig. 3.2 (c) shows the busyness distribution of Fig. 3.2 (b). It is obvious the busyness value is high in the sclera region/no vessel region. So the segmentation artifact can be recognized by applying a satisfactory threshold to the busyness image. The gray pixels in fig. 3.2 denote the removed artifact in adaptive thresholding based vessel segmentation.

3.3.2 Multi-scale adaptive thresholding based choroidal vessel segmentation

The choroidal vessel varies from several μm to hundreds-μm in diameter. Adaptive thresholding method with a fixed window size can not always provide a satisfactory segmentation results for vessels with different diameters. A large window can either over-estimate the vessel diameter or ignore the vessel signal, while a small window is unable to segment a vessel with a higher

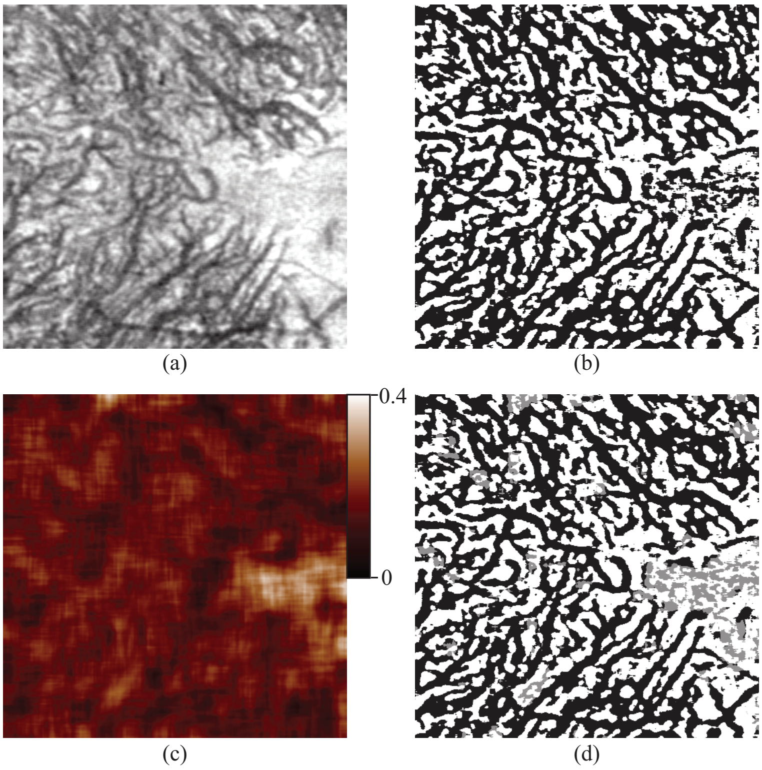

Figure 3.2: (a) OCT *en-face* slice. (b) Binary image obtained by adaptive local thresholding with a fixed window size. The white and black represent background and vessel, respectively. (c) Busyness distribution. (d) Result of artifact removal achieved by busyness filter. The light gray pixels are vessel artifact that is recognized and removed by busyness filter.

diameter than the window size in adaptive thresholding. To obtain segmentations to choroidal vessel with different diameters, I propose a multi-scale adaptive thresholding based choroidal vessel segmentation method. The final result is achieved by combination of the reliable choroidal vessel signal obtained by adaptive thresholding based segmentation with different window size.

Selection of reliable segmentation

The determined threshold can best separate the background and vessel when their area is similar in a local window because the local threshold is statistically determined. If background area is much larger than vessel area, the threshold would probably be close to the values of backgrounds. So adaptive thresholding with large window size often overestimate the diameter a thin vessels. Here I believe it becomes unreliable if the diameter of segmented vessel by adaptive thresholding method is lower than 1/5 of the window size. Those identified thin vessel should be properly segmented by a smaller window size.

A morphological process based procedure is customized to select the reliable vessel segmentation in output of adaptive thresholding with specified window size, w. Firstly, I reverse the binary image (making ”0” to be vessel and ”1” to be background) and remove the particles with diameter lower than 2 pixels. The purpose of this operation is to fill the small holes in the large vessels otherwise they can be regard as two adjacent thin vessels in following morphological analysis. Then, after reversion of the binary image, an open operation is performed using a circular structuring element with diameter of 0.2w. The vessels with a diameter lower than 0.2w will be erased while other vessels' preservation. Further, the vessel particles with Heywood circularity factors lower than 1.5 are remove in the binary image. This process rejects the vessel particles whose shape are close to round but not vessel pattern. Finally, the reliable vessel segmentation is preserved in the binary output.

In this procedure, I only consider the segmentation over-segmentation of thin vessel by a large window size but not insufficient segmentation in the opposite condition. This is because the insufficiently segmented signal can be fully covered by reliable segmentation using larger windows.

Multi-scale vessel segmentation combination

OCT signal in thick choroidal vessels, which mainly distribute in the Haller's layer, is much lower than that in medium and thin vessels close to the RPE because of signal attenuation as penetration depth and low backscattering coefficient of blood. Based on the assumption that the OCT signal in the medium and thin vessel area is much higher than that in thick choroidal vessel and sclera areas, I reasonable split the selected choroidal OCT volume into two parts, the thin and medium choroidal vessel region and the thick choroidal vessel and scleral region, using the Otsu's threshold intensity values of all pixels in one volume. The thin and medium vessel segmentation result is achieved by applying ”or” operation to the busyness filtered adap-

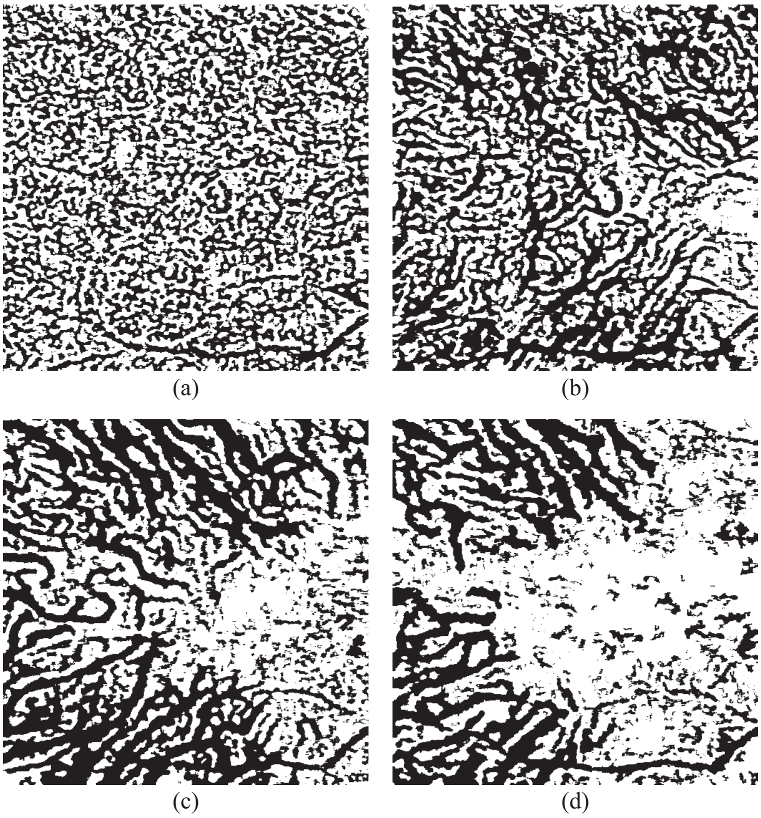
(a) (b)
(c) (d)

Figure 3.3: Choroidal vessel segmentation results corresponding to OCT *en-face* slices in Fig. 3.1.

tive thresholding results with adaptive thresholding window size of 94 μm and 47μm, while the large vessel segmentation is calculated as ”or” of that with window size of 375μm, 188μm, and 94μm. Finally, the volumetric choroidal vessel segmentation is realized by reconstructing the vessel pixels in this two regions. Figure 3.3 shows the vessel segmentation results corresponding to the OCT *en-face* slices shown in Fig.3.1.

3.3.3 Retinal vessel shadow rejection

The retinal vessels act as a cucoloris that casts a shadow in the choroidal OCT volume. This shadow signal appears in all of the *en-face* slices can be detected as choroidal vessel. Hence, this vessel pixels located in the retinal vessel shadow should be distinguished and rejected before the following choroidal vessel analysis.

The retinal vessel shadow can be the most clearly visualized in the hyper-reflective complex includes the RPE, and IS/OS layers. A projection of the hyper-reflective complex, as shown in fig. 3.4 (a), is obtained by averaging the intensity in the hyper-reflective complex segmented

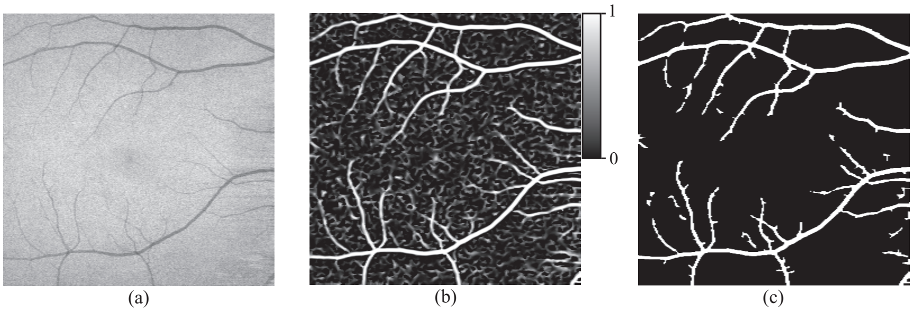

(a) (b) (c)

Figure 3.4: (a) *En-face* projection of the hyper-reflective complex obtained by averaging the intensity values in each A-lines. (b) Vessel structure is enhanced by Frangi filter. (c) Retinal vessel shadow segmentation.

in 3.2. After a anisotropic diffusion filter, I applied a Frangi filter to further enhance the vessel pattern from the background [89]. The nonlinear parameters of the Frangi filter are customized to discriminate the vessel from background by threshold 0.5. A close operation is also performed to the binary output to ensure a connective vessel network. Figure 3.4 (b) and (c) show the output of the Frangi filter and retinal vessel segmentation result, respectively. The segmented retinal vessel is masked to *en-face* slices so that the retinal vessel pixels are invalided in the choroidal volume. Note that the retinal vessel shadow segmentation result shown in Fig. 3.4 (c) is actually not an accurate vessel network but a slightly dilated area. This feature warrants a sufficient removal of the retinal vessel shadow in choroidal data.

3.4 Choroidal vasculature evaluation

3.4.1 Choroidal vessel diameter estimation

Normally, the vessel thickness can be determined by the distance of two surface in the cross-section direction. However, the orientation of choroidal vessel is highly randomly distributed and difficult to track so that its diameter cannot be directly measured in a standard way. Opening in morphology is the dilation of the erosion of a binary image by a structuring element. As mentioned in 3.3.2,it removes small objects from the foreground of a binary image. The vessel pixels are actually classified into two groups: vessel pixels with diameter higher or lower than the diameter of structuring element in open operation. Based on this idea, I estimate the vessel diameter by applying a serial of open operations. The diameter of structuring element in i-th open operation is set to d_i = i × d_1, where d_1 is the structuring element diameter in the first open operation and the maximum value of d_i should be higher than the maximum diameter of choroidal vessel.

In open operation, only a round-shape structuring element can equally estimate the vessel diameters with different orientation. However, if the structuring element is too small in a digital

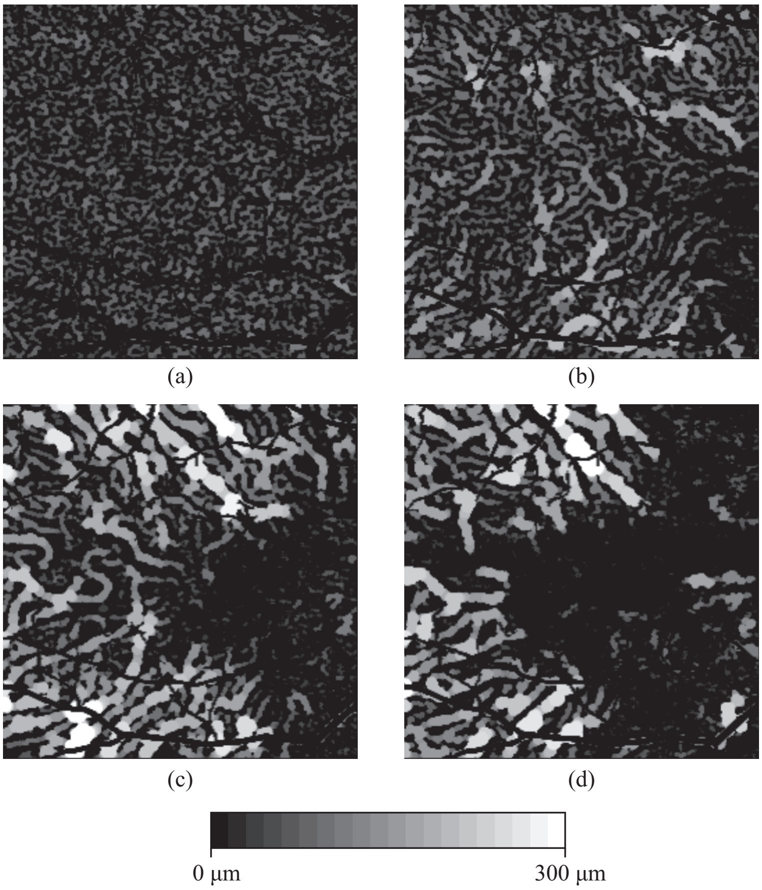
(a) (b) (c) (d)

Figure 3.5: Choroidal vessel diameter estimations corresponding to vessel segmentation results in Fig. 3.3. The black pixel denotes no vessel is detected and the retinal vessel shadow is removed.

image processing, the round model becomes a polygon. To guarantee a round shape structuring element with smallest diameter, I perform a 2D interpolation to increase the pixel density of the *en-face* slices. Then, a serial of open operations are implemented using structuring elements with diameter of d_i where i varies from 1 to 20. The increasing step of d_1 is 15 μm. Figure 3.5 shows the diameter estimation results corresponding to the OCT *en-face* slices shown in 3.1. The resolution of diameter estimation is determined by the diameter increasing step of structuring element. The choroidal vessel diameter can be quantitatively visualized in different layers.

3.4.2 Vascularized layer thickness measurement in the Choroid

The thickness of the choroidal vasculature is also measured by applying a active deformable surface model to the choroidal vessel diameter volume. I construct a 10 × 10 control point array in the *en-face* plane as shown in fig. 3.6 (a). A deformable surface, as shown in fig. 3.6 (b),

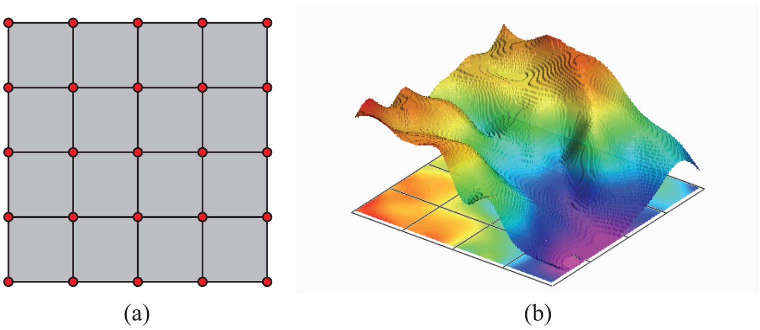
(a) (b)

Figure 3.6: Active deformable surface models. (a) 10 × 10 control points. (b) An example of deformable surface obtained by 2D interpolation to control point array.

is obtained by applying 2D bicubic spline interpolation to the control point array. The control points are initialized in the choroidal region and move along axial direction. Depth of the n-th control point from the RPE is determined by

$$D_n(i+1) = \begin{cases} D_n(i) + D_0 & for\ f_n(i) < -T \\ D_n(i) - D_0 & for\ f_n(i) < T \\ D_n(i) & for\ otherwise \end{cases} , \tag{3.2}$$

where i is current loop iteration number, D_0 is the axial pixel resolution of OCT system, T is a constant threshold, and $f(n)$ is the resultant that is defined as

$$f_n(i) = \alpha R_n(i) + \beta P_n(i) + \gamma G_n(i) \ , \tag{3.3}$$

where α, β, and γ are constant weight factors, and $R_n(i)$, $P_n(i)$, and $G_n(i)$ denote local rigidity, local pushing force, and gravity of control point, respectively. Local rigidity is quantitatively determined by the second derivative of the deformable surface. This term can reasonably keep the deformable flattened. The gravity, which is a constant, pulls the control points down from the RPE to the sclera, while the background pixels in the deformable surface provide a pushing force raising them. The posterior interface of the choroidal vasculature is obtained by arguing a balance solution of the deformable surface model iteratively. Associated with the the Bruch's membrane segmentation result, a 2D map of the choroidal vasculature can be finally obtained.

3.5 *In vivo* application of choroidal vessel characterization algorithm

The macular region was imaged *in-vivo* in healthy subjects by HP-OCT with 1-μm probe. The setup and parameters of this system have been described anywhere else. 6 mm × 6 mm area was

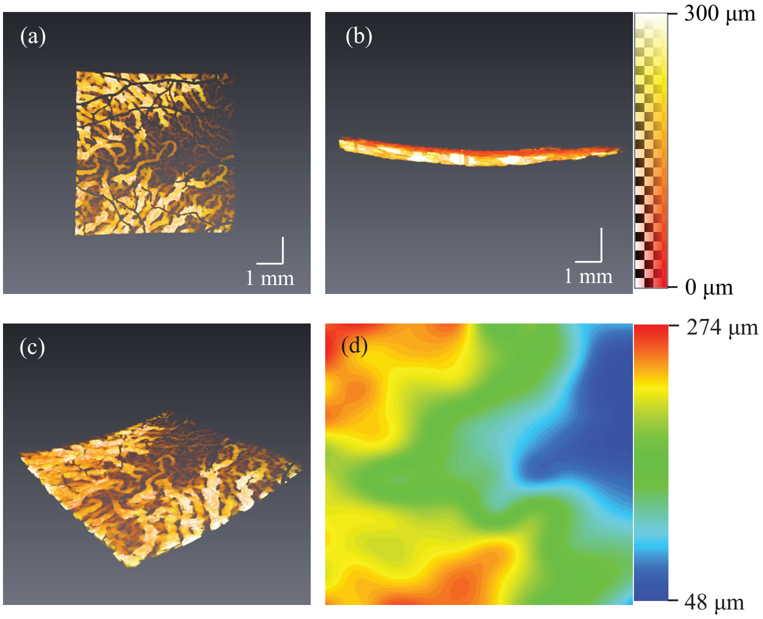

Figure 3.7: (a) ∼ (c) are top, side, and Bird's-eye views of a volume rendering images of choroidal vasculature. (d) Choroidal vasculature thickness map.

imaged with 2048 A-lines in one frame and 256 frames in one volume. The probe power on the cornea was around 1.8 mW.

An example of reconstructed three dimensional choroidal vasculature is shown in Fig. 3.7. The choroidal vessel has been recovered to its original spacial shape in the OCT volume. The color of voxels in those images denote the diameter of the vessel. The Sattler's and Haller's layer can be visualized as shown in Fig. 3.7 (b). It is clear that the thin vessels distributed just beneath the RPE while the thick vessels distributed in deeper layer. Figure 3.7 (d) shows the corresponding thickness map. Obviously, the entire thickness of choroidal vasculature is highly correlated to distribution of thick choroidal vessel.

Figure 3.8 illustrates distributions of choroidal vessel diameter versus depth from the RPE in two eyes of two subjects. The results show a obvious increasing tendency in choroidal vessel diameter distribution. This matches to our anatomical knowledge in the choroid. The mean diameter can somehow indicate the thickness of sub-layers in the choroid. In both examples, it appears a high gradient from 50 μm to 100μm. This might be the general depth range of interface of the Sattler's layer and Haller's layer. The choroidal vasculature indicated in Fig. 3.8 (c) and (d) is thicker than that in Fig. 3.8 (a) and (b). This difference mainly determined by the Haller's layer thickness. The mean diameter appears an abrupt local maximum around 270 μm in example shown in Fig. 3.8(a) and (b). This because the choroidal vasculature thickness is uneven distributed so that the vessel pixel number in deep layer is too low to correctly represent statistical parameters.

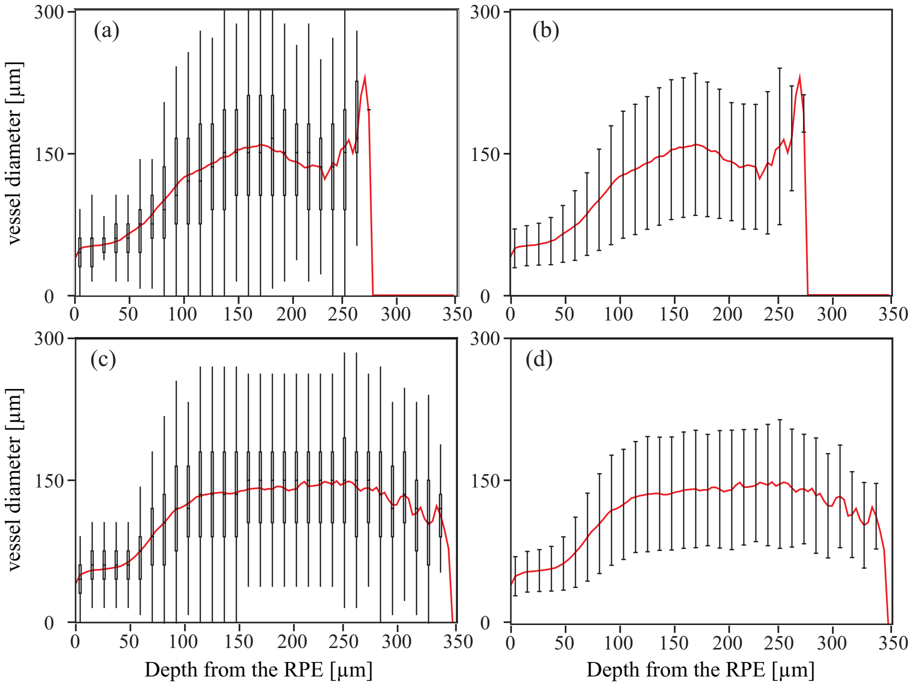

Figure 3.8: Plots of choroidal vessel diameter versus depth from the RPE in two subjects. Box and whisker plots (a)(c) and standard deviation plot (b)(d) exhibit the distribution of choroidal vessel diameter at a specified depth from the RPE. The red curves show the mean of choroidal vessel diameter.

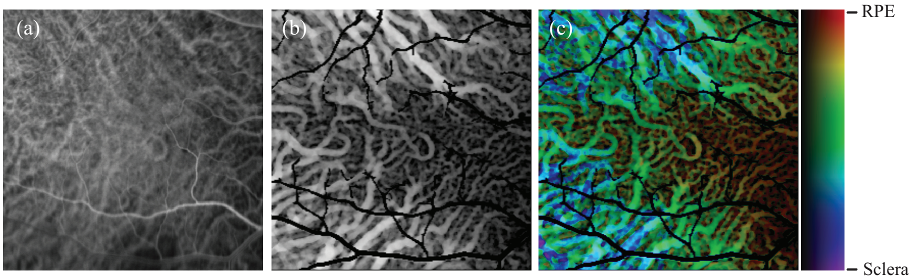

Figure 3.9: Comparison of ICGA (a), *en-face* projection of vessel diameter volume (b), and depth-resolved *en-face* projection of vessel diameter volume (c) of 6 mm × 6 mm macular region obtained from the same subject.

Two dimensional thick choroidal vessel network can be visualized in ICGA image as shown in Fig. 3.9 (a). However, the boundary of the thick vessel is unclear because of blocking effect from anterior thin vessels and dye leakage, and the thin choroidal vessel can hardly visualized because of low signal. ICGA-style projection of choroidal vessel diameter volume is created by averaging the diameter value in each A-line. Figure 3.9 (b) shows the *en-face* projection, in which square root of diameter average is taken to promote visualization. The thick choroidal vessel pattern is similar to that shown in ICGA image but visualization is significantly promoted. Thin vessel pattern appears in area without thick choroidal vessel. The retinal vessels are also distinguished and removed from projection image. Further, I also create a depth-resolved choroidal vessel projection as shown in Fig. 3.9 (c). The brightness of pixel is the same with Fig.3.9 (b) representing the vessel thickness. The hue value denote the average vessel depth, which is calculated as $\sum(\text{diameter} \times \text{depth})/\sum\text{depth}$ of pixels in each A-line. The pixel color from red to blue corresponds to the vessel depth from the RPE to sclera. Thickness and depth information is simultaneously visualized in depth-resolved projection of vessel diameter volume.

The choroidal vasculature thickness maps measured in 8 eyes of 4 healthy volunteers are shown in Fig 3.10. Maps in the same row indicates the choroidal vasculature thickness distribution in the oculus dexter and sinister eyes of a same volunteer. A thinner choroidal vasculature thickness in the nasal area than the temporal area is observed in all of 8 maps. Patterns of the choroidal vasculature thickness maps are generally symmetric in two eyes of the same subject except the third subject whose results are shown in the third row, but a clear pattern difference appears between results in different subjects. Figure **??** shows a B-scan image extracted from the OCT volume measured in oculus dexter eye. A block without any vessel-like pattern appears between the sclera and choroidal vasculature as marked as a red dashed ellipse. No vessel-like structure is observed in this block area. This block has also been observed in OCT images obtained in the same eye and validated to be low in birefringence in Ref. [74], hence it is not a part of the sclera. Existence of this kind of blocks and their distribution seems to be a reason to asymmetric pattern of the choroidal vasculature maps.

Figure 3.12 shows depth-resolved projection of vessel diameter volume corresponding to choroidal vasculature thickness maps in Fig 3.10. Note that the hue only shows a relative but not absolute depth of the choroidal vessel. It is clear that the choroidal vasculature thickness pattern is highly correlated to the thick choroidal vessel distribution pattern. Distribution of the thick choroidal vessel is different between subjects, and there is no evidence indicate this pattern is constant as time in one eye in our best knowledge. Variation of the thick choroidal vessel distribution can be an factor that affects the local choroidal thickness other than thinning or reduction of the choroidal vessel. Hence, we believe volumetric/depth-resolved visualization and thickness mapping of the choroidal vasculature can provide a superior analysis to the choroidal vasculature properties than the thickness measurement performed in B-scan images or A-lines.

3.6 Discussion

ICGA is commonly used to examine choroid vasculature in clinics. It is uncomfortable but still safe in most cases, but some adverse reactions can limit its application. ICGA are mostly utilized to visualization abnormalities in the choroid, but defy common quantitative analysis of the choroidal vasculature because of two dimension imaging feature and low vessel contrast. Optical coherence angiography, or optical doppler angiography, yield three dimensional vessel structure invasively. However, its depth resolution is quite limited in the choroid, especially in Haller's layer because of low sensitivity and shadow effect of Doppler phase. The proposed algorithm direct analyses the structure information obtained by HP-OCT, providing 3D volume rendering visualization of the choroidal vessels as well as vessel diameter and entire vasculature thickness information. Yet, this structural information based method do not provide functional information such as leakage. Hence, it is not alternative but complementary method for other techniques.

As referred in Sec. 3.3.2, the choroidal vessel can be properly segmented only if the vessel diameter is close to half of the window size in adaptive thresholding. The minimum window size was 47 μm in multi-scale adaptive thresholding based choroidal vessel segmentation, so the diameter of the most thin vessel that can be properly segmented is around 24 μm. If the vessel thinner than this limitation, its diameter can be over-estimated. So the segmentation result in the choriocapillaris is not as reliable as that in the Sattler's and Haller's layer. Further decreasing of the window size cannot promote the accuracy of the segmentation because of the limitation of the transversal resolution of the OCT system. Adaptive optics OCT measurement might supplement some additional information to the choroidal vasculature analysis.

Precision of vessel diameter estimation is directly determined by structuring element diameter increasing step between two adjacent open operations. A small increasing step of structuring element diameter results in a high precision in vessel diameter estimation. However, it requires more open operations so longer processing time since the maximum diameter is fixed. The

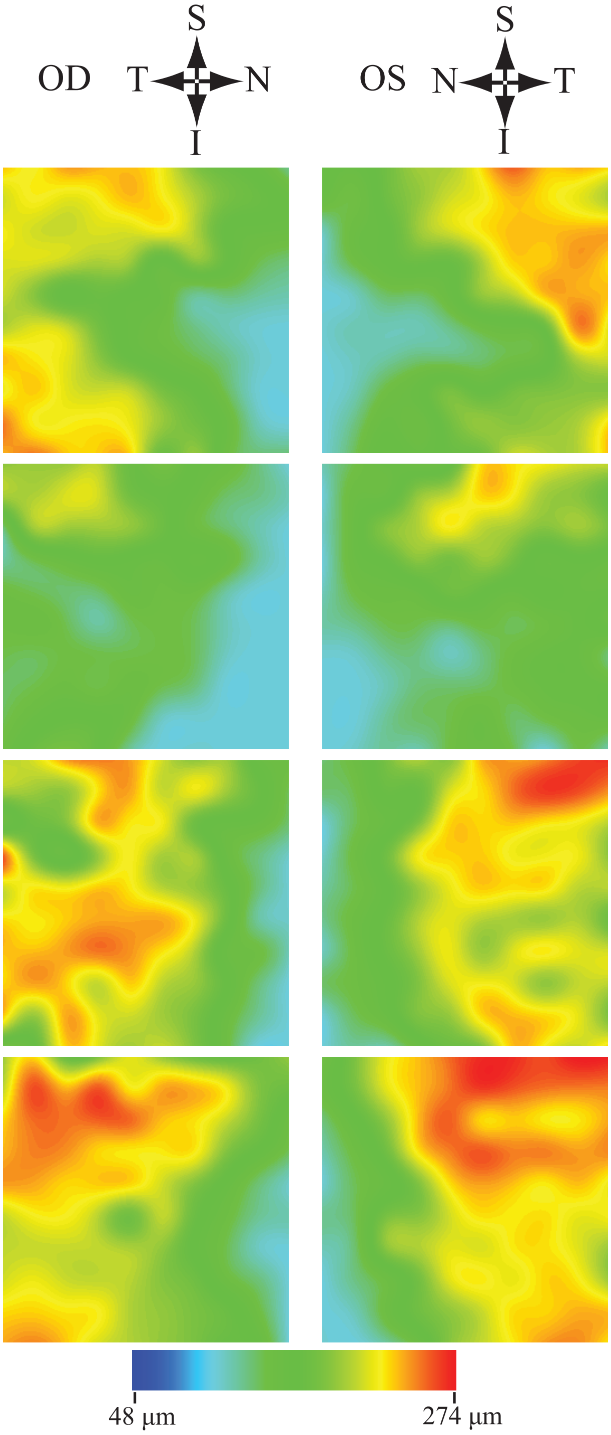

Figure 3.10: Choroidal thickness maps obtained in 8 eyes of 4 healthy volunteers. The maps in a same row were acquired from the two eyes of a single subject. OS/OD: Oculus dexter/sinister; N: Nasal; T: Temporal; S: Superior; I: inferior. Black dashed line in left image in the third row denoted the position of B-scan shown in 3.11.

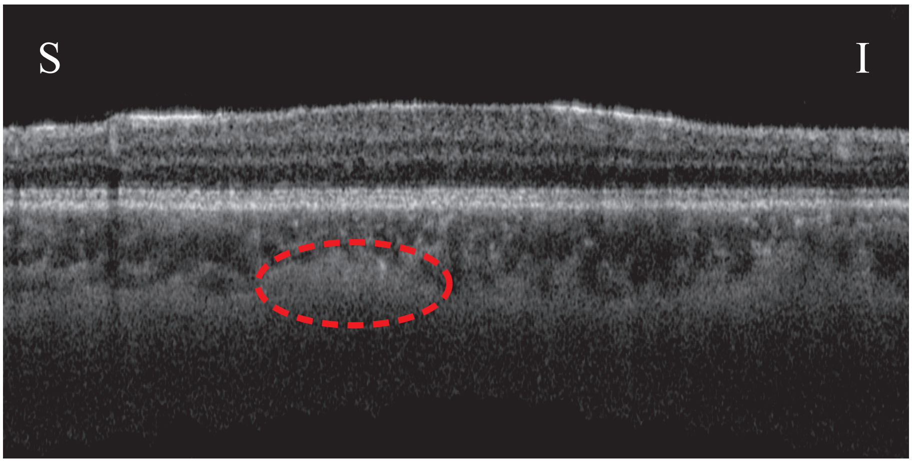

Figure 3.11: A B-scan image extracted from OCT volume corresponding to left image in the third row in 3.10.

trade-off between calculation time and vessel diameter estimation should be balanced.

In current status, it takes about 4 second to segment an *en-face* resized to 256 × 2048 pixels in program written in LabVIEW (LabVIEW 2011 for 64-bit Windows 7) on Intel CORE i7 CPU Q720 at 1.6GHz with 8-G RAM. Another 20 second is required to estimate the vessel diameter using 20 open operation with initial diameter of 5 pixels and diameter increasing step of 5 pixels in a binary slice resized to 2048 × 2048 pixels. The open operation is substantively achieved by convoluting the image by structuring element in Fourier domain. The calculation time increases as the pixel number of structuring element. The calculation time can be significantly shorten if decreasing the pixel number of input image. However, the structuring element diameter should also reduce. A digital image with low pixel number cannot provide a structuring element approaching to round shape, which is necessary for isotropic diameter estimation.

3.7 Summary

This chapter introduces an automated algorithm to segment and evaluate the choroidal vessel in volumetric data provided by HP-OCT in this chapter. The three-dimensional choroidal vessel network is segmented based on intensity contrast from the background tissue. The following analysis to the segmented vasculature can provide both the choroidal vessel thickness and the entire choroidal vasculature thickness. Enhanced visualization and characterization of the choroidal vessel are achieved in volumetric HP-OCT data.

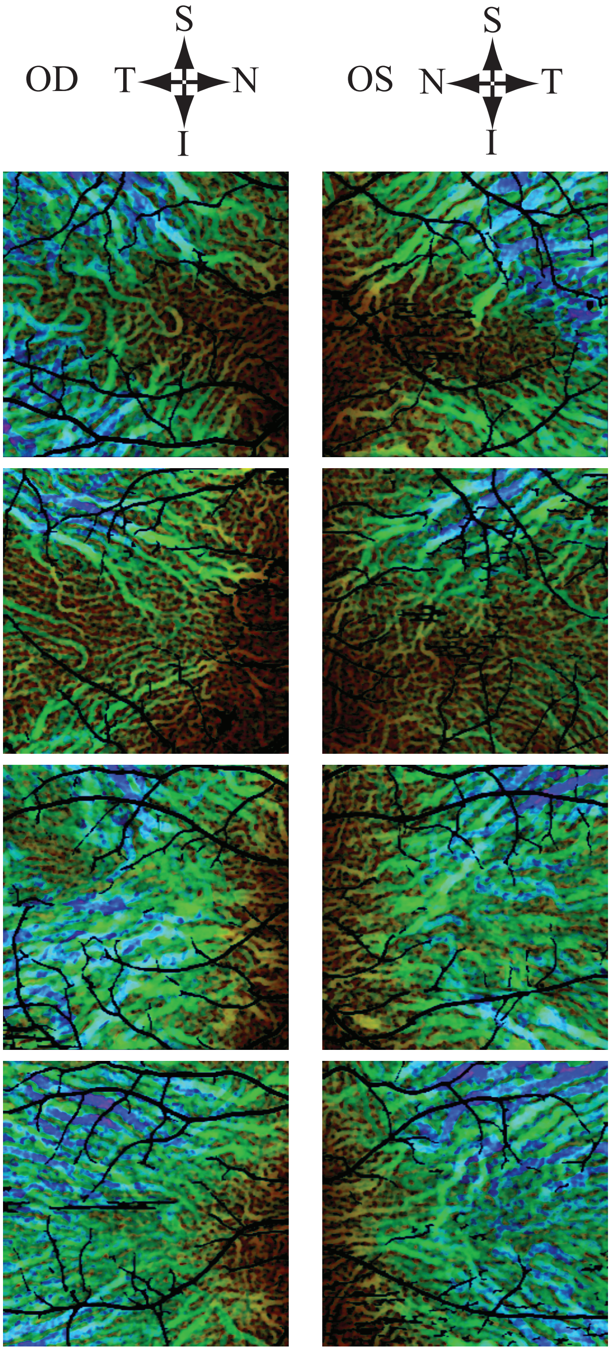
OD
S
T
N
I
OS
S
N
T
I

Figure 3.12: Depth-resolved projections of vessel diameter volume corresponding to the choroidal thickness maps in 3.10.

Chapter 4

Conclusion

This dissertation presented several algorithms for advanced image processing of OCT images obtained in deep layers of the posterior segment of the eye. All of the researches have been concentrated on investigation of the choroid, which is an ocular structure accounting for several essential functions. Two projects have achieved fully automatic measurement of the ”real” thickness of the choroid and fully automatic characterization of choroidal vessel in OCT data acquired by OCT systems with 1-mum wavelength, respectively. These works have been highly motivated by methodological development for diagnosis of ophthalmic diseases.

An automated choroidal thickness measurement method by PS-OCT was developed in the first project. Based on histological properties of the layers around the choroid, the anterior and posterior boundaries of the choroid are automatically segmented based on intensity and phase retardation contrasts provided by PS-OCT simultaneous. This work challenged the current intensity information based choroidal thickness measurement methods, providing an access to the ”real” thickness of the choroid.

The second project proposed a framework to analyse the choroidal vessel information. The choroidal vessel was segmented by a customized multi-scale adaptive thresholding method in *en-face* slices extracted from a OCT volume. Then, the choroidal vessel thickness and the entire choroidal vasculature thickness are estimated by a morphological operation based analysis and a deformable surface model, respectively. The reconstructed 3D choroidal vasculature and depth-resolved vessel projection offer both enhanced visualization and quantitative characterization of the choroid. The result of this framework demonstrated enhanced visualization of the choroidal vasculature as well as depth information of the choroidal vessel.

This two projects offered morphology of the choroid in macrocosmic and microcosmic view, providing comprehensive parameters describing condition of the eye related to this layer. Those information might be useful to promote pathological understanding and clinical diagnosis of several circulation-related ocular diseases. Efficiencies of both methods have also been validated in *in vivo* OCT data, demonstrating high practicabilities for future clinical application.

Appendices

Appendix A

Calibration Protocol for Resonalt Electro Optic Polarization Modulator

A.1 Introduction and Purpose

Jones matrix PS-OCT utilized in Chap. 2 relays on modulation of phase of a single polarization component of the source or probe beam by an electro-optic modulator (EOM) [50]. We had used several types of EOM including bulk EO crystal driven at non-resonant slow frequency (New Focus), wave-guide EO modulator (EO Space), and a resonant EOM with high-frequency ($\sim$ a few ten mega Hertz) driving. Among these EOMs, the resonant EOM has particular difficulty for its characterization. This is mainly because the modulation property, which is mainly indicated by the relationship between applied voltage and the depth of modulation, is becoming a function of modulation frequency.

This appendix aims at describing step-by-step protocol to characterize the resonant EOM for polarization modulation of Jones PS-OCT.

More concretely, we will obtain a function $f(V)$ which relates the modulation depth of EOM (A_0) and the driving voltage of EOM, in practice which is the output amplitude of a sinusoidal wave generated by a function generator driving the EOM as $A_0 = f(V)$. And then define the optimal driving amplitude of the EOM which enables the modulation depth of 2.405 radians which is the optimal modulation depth for our Jones PS-OCT.

A.2 Experimental Setup

For the characterization of a resonant EOM, we use a simple optical setup shown in Fig. A.1. In this setup, incident light first path through 90-deg polarizer for cleaning-up, passing an EOM under test. Here the optic axis of this EOM is aligned to 45 degrees. The output from the EOM passes an analyzer with 0-deg orientation.

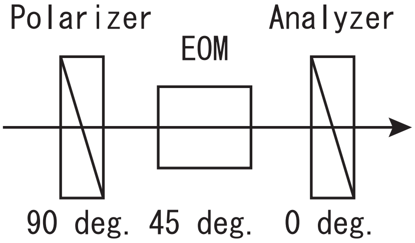

Figure A.1: The optical scheme for the caricaturization of a resonant EOM.

For the data acquisition, the light source utilized is a wavelength sweeping source which is also utilized for the PS-OCT and the EOM is modulated with a modulation frequency identical to the PS-OCT. The output optical intensity after this polarization is detected by a high-speed detector and recorded by a oscilloscope as the wavelength is scanned.

A.3 Theory and Data Processing

We first assume the incident light is a static (non-scanning) 90-deg. polarized light. The Jones vector of this incident light becomes

$$E_{in} = \begin{bmatrix} 0 \\ 1 \end{bmatrix} \tag{A.1}$$

The electric field after this Jones matrix of the above mentioned system becomes

$$E_{out} = \begin{bmatrix} 1 & 0 \\ 0 & 0 \end{bmatrix} \begin{bmatrix} \exp(+i\delta/2) & 0 \\ 0 & \exp(+i\delta/2) \end{bmatrix} \begin{bmatrix} 0 & 0 \\ 0 & 1 \end{bmatrix} \begin{bmatrix} 0 \\ 1 \end{bmatrix}, \tag{A.2}$$

where δ is the retardation of the EOM. The output optical intensity then becomes

$$I_{out}(t) = E_{out}^{\dagger} E_{out} = \frac{1}{4} \sin^2 \frac{\delta}{2} \tag{A.3}$$

where the superscript of † indicates transpose of complex conjugate.

The retardation of the EOM is modeled as follows.

$$\delta = \varphi + A_0 \cos(\omega_m t + \theta), \tag{A.4}$$

where φ is the offset phase retardation defined by the EOM device, $A_0 \equiv f(V)$ is the phase modulation depth with a voltage amplitude of driving RF signal applied to the EOM of V and $f()$ is an unknown function which relates V and A_0, and θ is a temporal offset of the driving RF signal. t is a variable representing time.

By substituting Eq. (A.4) to Eq. (A.3), the I_{out} becomes

$$I_{out}(t) = \frac{1}{4} \sin^2 \left[\frac{\varphi + A_0 \cos(\omega_m t + \theta)}{2} \right] \tag{A.5}$$

Because we are going to use a wavelength-sweeping light source, the incident light power is not a constant of time but a function of time. We model this time-dependent incident power as $S(t)$. In addition, the optical intensity measurement can have a constant background by some reasons. We represent this constant background by β. By using $S(t)$ and β, the equation of output intensity Eq. (A.5) is modified to

$$I'_{out}(t) = S(t)\frac{1}{4}\sin^2\left[\frac{\varphi + A_0\cos(\omega_m t + \theta)}{2}\right] + \beta \tag{A.6}$$

As we discussed above, this equation properly models the output from the optical setup of Fig. A.1. By observing this equation, one can immediately find that this equation contains five unknown parameters of φ, A_0, ω_m, θ, and β and one unknown function of $S(t)$

In our calibration strategy, we first cancel the effects of the unknown function of $S(t)$ from the experimental data, and then apply nonlinear least square fitting (Marquardt-Levenberg algorithm) to identify residual parameters.

The cancellation of $S(t)$ is performed in Fourier domain. To understand this operation in the Fourier domain, first Eq. (A.6) is rewritten by using a half-angle formula as

$$I'_{out}(t) = S(t)\left[\frac{1-\cos(\varphi + A_0\cos(\omega_m t + \theta))}{2}\right] + \beta \tag{A.7}$$

$$= \frac{1}{2}S(t)\left\{1 - \cos\varphi\cos\left[A_0\cos(\omega_m t + \theta)\right] - \sin\varphi\sin[A_0\cos(\omega_m t + \theta)]\right\}$$

This equation is further expanded to

$$\begin{aligned} I'_{out}(t) &= \frac{1}{2}S(t) \times \\ &\left[1 - \sum_{n=0}^{\infty}\varepsilon_n(-1)^n J_{2n}(A_0)\cos\varphi\cos(2n\omega_m t + 2n\theta)\right. \\ &\left. + \sum_{n=0}^{\infty} 2(-1)^n J_{2n+1}(A_0)\sin\varphi\cos((2n+1)\omega_m t + (2n+1)\theta)\right] + \beta \end{aligned}$$

where ε_n = 1 for $n = 0$ and 2 for others. The following formula were utilized to derive these equations.

$$\cos(z\cos(\rho)) = \sum_{n=0}^{\infty}\varepsilon(-1)^n J_{2n}(z)\cos(2n\rho) \tag{A.8}$$

$$\sin(z\cos(\rho)) = \sum_{n=0}^{\infty} 2J_{2n+1}(z)\cos((2n+1)\rho) \tag{A.9}$$

The numerical Fourier transform of the obtained signal can be mathematically modeled by the Fourier transform of Eq. (refeqn:Iout4) as

$$\begin{aligned} I'_{out}(t) &= \beta\delta(\omega) + \frac{1}{2}\mathcal{F}\left[S(t)\right] * \\ & \quad \mathcal{F}\left[1 - \sum_{n=0}^{\infty} \varepsilon_n (-1)^n J_{2n}(A_0)\cos\varphi\cos(2n\omega_m t + 2n\theta)\right. \\ & \quad \left. + \sum_{n=0}^{\infty} 2(-1)^n J_{2n+1}(A_0)\sin\varphi\cos\left((2n+1)\omega_m t + (2n+1)\theta\right)\right] \end{aligned}$$

where $\mathcal{F}[\ ]$, $\delta(\ )$, and $*$ represent Fourier transform, delta function, and convolution. ω is the Fourier pair of t. According to this equation, the important part of this signal, which is appeared at the second and third lines of this equation, only contains the frequency components of the integer-multiples of $\omega_m t$. And all harmonics are equally convolved with $\frac{1}{2}\mathcal{F}[S(t)]$.

Hence, the following operation to the experimentally obtained data will clean up the effect of $S(t)$.

$$\begin{aligned} I''_{out}(t) &\equiv \mathcal{FFT}^{-1}[\mathcal{FFT}[W(t) \times I'_{out}(t)] \times \mathrm{comb}(\omega/\omega_m)] && \text{(A.10)} \\ &= \gamma \times \sin^2\left[\frac{\varphi + A_0\cos\left(\omega_m t + \theta\right)}{2}\right] + \beta && \text{(A.11)} \end{aligned}$$

where $\mathcal{FFT}[\ ]$ is fast Fourier transform, γ is a constant and $W(t)$ is a window function for FFT that is typically a Hamming window. By some practical reasons, in our particular implementation, we rather use the following operation than Eq. A.10.

$$\begin{aligned} I''_{out}(t) &\equiv \mathcal{FFT}^{-1}[\mathcal{FFT}[W(t) \times I'_{out}(t)] \times \{\mathrm{comb}(\omega/\omega_m) - \delta(\omega)\}] && \text{(A.12)} \\ &= \gamma \times \sin^2\left[\frac{\varphi + A_0\cos\left(\omega_m t + \theta\right)}{2}\right] + \beta' && \text{(A.13)} \end{aligned}$$

One can immediately see that the difference between these two equations are the difference in the constant offset. Since this constant offset is out of our interest, this difference does not have significant effect.

A.4 Nonlinear Least Square Fitting

After cleaning the effect of $S(t)$, the experimental data were fit by Eq. A.12 with six unknown parameters of γ, φ, A_0, ω_m, θ and β'. The fitting was done by Marquardt-Levenberg algorithm (Nonlinear Curve Fit VI of LabVIEW 2010), and 256 data-points close to the center of the spectrum was used. The first estimation of the parameters were manually selected to roughly fit the theoretical curve to the data. This manual selection of first estimation is important to avoid sub-optimal solution.

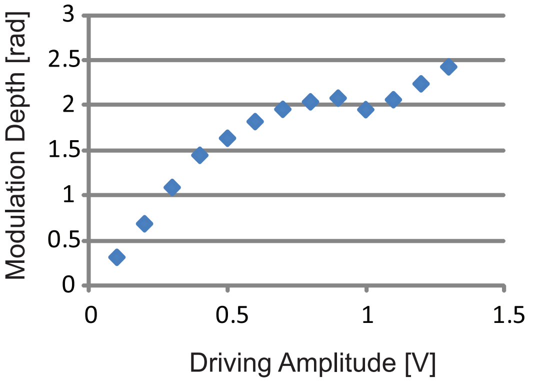

Figure A.2: Experimentally obtained relationship between the modulation depth (A_0) and the driving amplitude (V).

A.5 Experiment and Results

We applied the above-mentioned method to characterize a bulk EOM for 1-μm range manufactured by New Focus. The experiment was done with a light source of Santec HSL-1000 with a center wavelength of 1060 nm.

We performed the above mentioned measurements with the voltage amplitude (V) of the sinusoidal wave generated by a function generator which drives the EOM from 0.1 V to 1.3 V with 0.1 V spacing. The data was analyzed by the operation described by Eq. (A.12).

The obtained parameter of A_0 is then plotted as a function of V as shown in Fig. A.2. This plot represents the function $A_0 = f(V)$. Although Fig. A.2 shows highly nonlinear shape, the curve appeared as linear at the region $V > 1$, and this region covers the modulation depth of our interest of 2.405 radians. Hence, we apply a standard least square fit to the data points of V = 1.1, 1.2 and 1.3 [V] with a linear model, and obtained the following relationship between A_0 and V

$$A_0 = 1.8163V + 0.0596 \tag{A.14}$$

This equation finally indicates the optimal driving voltage of our EOM of 1.2913 [V] for 2.405-radian modulation depth.

A.6 Summary

In summary, the optimal modulation depth for a bulk New Focus EOM used in the PS-OCT in chap. 2 was measured to be 1.2913 V without signal amplification by RF amplifier. For another EOM in PS-OCT system, the optimal driving voltage can also be determined by the method proposed above.

Appendix B

Monte-Carlo-based phase retardation estimator for PS-OCT

B.1 Background and purpose

As mentioned in 2, PS-OCT is a functional extension of conventional OCT possessing all the original advantages. It enables both conventional backscattering tomography and birefringence tomography [42–45]. Tissue birefringence is strongly associated with the structural properties of biological tissues; hence, PS-OCT has been adopted for imaging skin [90–93], cartilage [94], teeth [95], and the anterior and posterior segments of the eye [46, 47, 60, 96–99].

Phase retardation is an important birefringent property of tissue, and it is widely employed to visualize PS-OCT images. It is a cumulative quantity that rotates in phase along the depth if the sample has birefringence while it remains constant if the sample has no birefringence. In biological tissues, micro-structural changes such as fibrosis, inflammation, and canceration can result in the alteration of phase retardation [98–100]; hence, the phase retardation image is of significant diagnostic importance. However, as reported in several studies, phase retardation measurements can be drastically affected by detection noise in PS-OCT [53, 101]. A standard mean estimator, i.e., average, cannot provide an appropriate estimation of phase retardation, and it significantly reduces the utility of PS-OCT for quantitative measurement [53].

Almost all PS-OCT algorithms derive phase retardation from multiple complex OCT signals. In the real and imaginary parts of the raw OCT signal, the noise distribution is reasonably assumed to be Gaussian centered at a true value. However, in general, the derivation of phase retardation from the raw OCT signals is complicated and, sometimes, nonlinear. This elaborates derivation process drastically complicates the analytic investigation of noise distribution in phase retardation.

As is widely known, Monte-Carlo simulation is a powerful tool for investigating stochastic processes of elaborate systems, and it has been widely employed for the analysis of the optical scattering property of biological tissues [102], theirs polarization dependency [103], and imaging modalities based on optical scattering, including diffusion tomography [104], photoacoustic tomography [105], and OCT [106]. The Monte-Carlo method has also been employed to investigate the noise property of phase retardation measurement in PS-OCT [53]. In this study, it was shown that the noise distribution in phase retardation is neither Gaussian nor symmetric. This is partially because the measurement range of phase retardation of PS-OCT is typically limited from 0 to π; hence, phase retardation signals less than zero or greater than π will be aliased in the 0 to π range. Because of this asymmetric distribution, both the mean and the mode include a systematic error, and they cannot provide a correct estimation of true phase retardation. Currently, this systematic error is minimized by enhancing the signal-to-noise ratio (SNR) of PS-OCT. However, to have a reasonably small error, a very high SNR, typically more than 20 dB, is required.

The objective of this appendix is to propose a method that reduces the systematic error in measurement and to relax the harsh SNR requirement for accurate phase retardation detection.

B.2 Monte-Carlo-based phase retardation estimator

The Monte-Carlo-based (MCB) phase retardation estimator proposed in this appendix is specifically designed for Jones matrix PS-OCT. For Jones matrix detection, two incident polarization states are required. These two spectra were detected by a polarization diversity (PD) detection unit, in which horizontal and vertical polarization components of the spectral interference signals are independently detected by two detectors.Then, both polarization components are detected by both the horizontal and the vertical detectors. The signals with different incident polarization states were demultiplexed by frequency shift or spacial shift method. The demultiplexed spectra were processed using a standard SS-OCT algorithm, and four OCT signals were obtained. Here, the OCT signals are denoted by $I_{0,H}(z)$, $I_{1,H}(z)$, $I_{0,V}(z)$, and $I_{1,V}(z)$, where the subscripts 0 and 1 denote non-modulated and modulated signals and the subscripts H and V denote horizontal and vertical polarization states of the PD detector, respectively. Then, the cumulative Jones matrix at a particular point in the sample $J_s(z)$ is obtained as

$$J_s(z) = J_r(z) J_{in}^{-1}, \tag{B.1}$$

where $J_r(z)$ and J_{in} are the raw Jones matrix measured at the point of interest and the Jones matrix measured at the surface of the sample, respectively [52]. By using the OCT signals, these matrixes are defines as

$$J_r(z) = \begin{bmatrix} I_{0,H}(z) & I_{1,H}(z) \\ I_{0,V}(z) & I_{1,V}(z) \end{bmatrix}, \tag{B.2}$$

$$J_{in} = \begin{bmatrix} I_{0,H}(z_0) & I_{1,H}(z_0) \\ I_{0,V}(z_0) & I_{1,V}(z_0) \end{bmatrix}, \tag{B.3}$$

where z and z_0 are the depth positions of the point of interest and the surface, respectively. In practice, J_{in} is a Jones matrix of the input fiber of the interferometer; hence, the effect of fiber birefringence is canceled by Eq. (B.1).

The round-trip phase retardation, $\delta_M(z)$, is obtained by matrix diagonalization [53] or by a trace method [107]. In this paper, we use the trace method represented by Eq. (B.4) rather than matrix diagonalization because it enables faster calculation.

$$\delta_M(z) = 2\cos^{-1} \frac{\left| \mathrm{tr} J_s(z) + \frac{\mathrm{det} J_s(Z)}{|\mathrm{det} J_s(Z)|} tr J_s^{\dagger}(z) \right|}{2\left[\mathrm{tr}\left(J_s^{\dagger}(z) J_s(z) \right) + 2\left| \det J_s(z) \right| \right]^{1/2}}, \tag{B.4}$$

where tr, det, and † denote the trace, determinant, and complex conjugate transpose, respectively. In this paper, the raw phase retardation $\delta_M(z)$ is expressed as the measured phase retardation.

Numerical simulations are performed to investigate the error and noise properties of phase retardation measurement. In the simulations, the noise is described using the same model as that used in a previous study [53]. Thus, the raw OCT signals, including $J_r(z)$ and $J_{in}(z)$, are modeled as the summation of the true Jones matrix and additive complex noise as

$$\begin{bmatrix} I_{0,H}(z) & I_{1,H}(z) \\ I_{0,V}(z) & I_{1,V}(z) \end{bmatrix} = \begin{bmatrix} S_{0,H}(z) & S_{1,H}(z) \\ S_{0,V}(z) & S_{1,V}(z) \end{bmatrix} + \begin{bmatrix} N_{0,H}(z) & N_{1,H}(z) \\ N_{0,V}(z) & N_{1,V}(z) \end{bmatrix}, \tag{B.5}$$

where Ss denote the true values of the OCT signals, and Ns denote complex noise in each channel. The real and imaginary parts of the noise follow zero-mean Gaussian distributions. The noises are totally decorrelated with each other, even though all of them are assumed to have identical standard deviations.

As shown in Eqs. (34)-(39) and Fig. 2 of Ref. 53, the noise property is described as a function of the effective SNR (ESNR; γ) rather than the SNR of each detection channel. The ESNR is defined as

$$\frac{1}{\gamma} = \frac{1}{4}\left(\frac{1}{\mathrm{SNR}_{s,0}} + \frac{1}{\mathrm{SNR}_{s,1}} + \frac{1}{\mathrm{SNR}_{r,0}} + \frac{1}{\mathrm{SNR}_{r,1}} \right). \tag{B.6}$$

$SNR_{s,i}$ and $SNR_{r,i}$ are defined as the ratio of signal energy (signal intensity) of the i-th incident light and noise energy of the i-th detection channel at the point of interest (denoted by the subscript s) and surface of the sample (denoted by the subscript r), respectively. Because of this property, we utilize ESNR rather than the SNR of each detection channel in the following analysis.

It should be noted that here we follow the definition of SNR of Jones matrix OCT described in Section 3.1.1 of Ref. 53. In this definition, the signal is the summation of the signal energies of all detections for a single incident polarization state, while the noise is defined as the noise level in each single detection. In our Jones matrix PS-OCT, two detectors, i.e. for horizontal and vertical polarization states, are utilized for polarization diversity detection. When we measure a void region, the signal energy detected by a single detector is equivalent to the noise energy.

According to the above mentioned definition, signal is the summation of the signal energies of the two channels, each of which is equivalent to the noise energy in this case. Hence the ESNR measured at a void region (noise region) becomes around 3 dB. This pseudo increasing of SNR is appeared only at a very low signal region.

The phase retardation measurements and numerical simulation were performed for a one-eighth wave-plate (EWP) and a quarter wave-plate (QWP), whose round-trip phase retardations are $\pi/2$ and π, respectively. For the wave-plates measurement, a tunable neutral density filter was located in a sample arm to control the incident power and hence SNR. 2^{13} A-lines were acquired for each SNR configuration. The intensity of OCT signal in air was averaged to obtain the noise floor of each detection channels, and the SNR and ESNR were calculated for the successive estimation of phase retardation. For each simulation, 2^{13} Monte-Carlo trials were performed. Figure B.1 shows the distribution of the raw measured/simulated phase retardation, δ_M, obtained from numerical simulations (left column) and experiments (right column) using an EWP (first and second rows) and a QWP (third and fourth rows). The histograms show good agreement between the simulations and the experiments. These results validate the proposed Monte-Carlo model.

Figure B.1 also shows that the distributions are asymmetric. This asymmetry is shown more quantitatively in Fig. B.2, where the skewness of the distributions of the true phase retardations (δ_T = 0, $\pi/6$, $\pi/3$, $\pi/2$, $2\pi/3$, $5\pi/6$, π radians) is plotted against ESNR. The skewness is defined as the third moment about the mean divided by the third power of standard deviation, and is one of the statistical measures of asymmetric level of prbability density function. Each distribution was obtained using a Monte-Carlo simulation with 2^{21} trials. For $\delta_T = 0$ and π, the skewness is not zero in nearly the entire ESNR range. Since skewness becomes zero for a symmetric distribution, these non-zero values of the skewness indicate that the distributions of $\delta_T = 0$ and π are not symmetric for any ESNR. For other δ_T, the skewness is nearly zero, i.e., the distribution is symmetric for high ESNR. However, the distribution becomes asymmetric for the ESNR less than around 20 to 25 dB. These asymmetries may be attributed to the aliasing at the perimeters of the measurement range and to the nonlinear relationship between the Jones matrix and the phase retardation.

Because of these asymmetries, the mean of the distribution cannot give a reasonable estimation of the true phase retardation δ_T. The mean of the simulated δ_M corresponding to several δ_T values are plotted against ESNR, as shown by the red curves in Figure B.3. The curves are obtained by averaging 2^{16} trials of δ_M obtained by the Monte-Carlo simulation. The mean of δ_M deviates from the true value (dashed lines) and approaches around 2.15 rad as ESNR decreases.

Conventionally, mean and maximum likelihood estimators have been utilized for quantitative estimation of polarization [47]. However, the asymmetric distribution presented above implies that these standard estimators do not provide appropriate estimations. This is because these estimators assume symmetric distribution of measured values. To overcome this problem, we propose an MCB estimator that involves a two-step estimation algorithm consisting of a non-

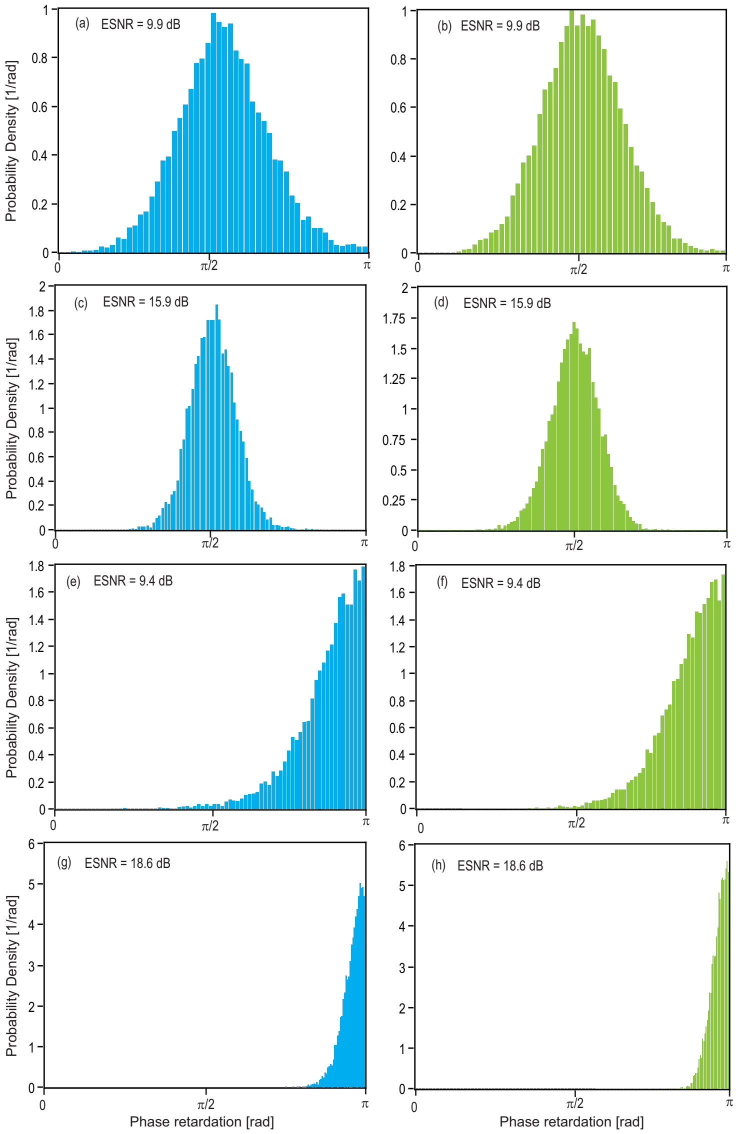

Figure B.1: Comparison of the measured phase retardation distribution with different $ESNR$ in the simulation and experiment. The sample is an eighth-waveplate in (a)-(d) and a quarter-waveplate in (e)-(h). (a),(c),(e), and (g) show the results of numerical simulation and (b),(d),(f), and (h) are the experimental results. The marked $ESNR$ values denote the mean $ESNR$ in each experiment or simulation.

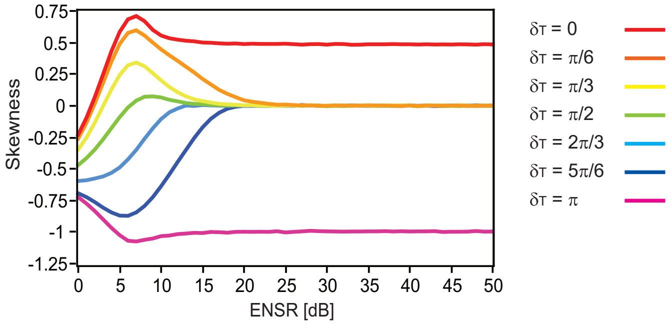

Figure B.2: Skewness of the distribution of phase retardation (δ_M) obtained by Monte-Carlo simulation for several true phase retardations.

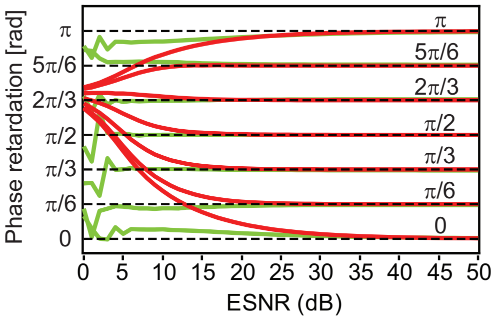

Figure B.3: Estimations of several set true phase retardations using 2^{16} trials of the measured phase retardation. The red and green solidlines denote the estimation results using mean and 4th order MCB estimators, respectively. The black dashed lines denote the true values.

linear distribution transform and a conventional mean estimation.

The first step of our MCB estimator is the distribution transform. We assume a transform function $f(\delta_M)$ that transforms measured raw phase retardation δ_M into transformed phase retardation, δ_E, for further estimation. The ensemble average of δ_E approaches the true phase retardation δ_T as the number of samples increases;

$$\delta_T \simeq \langle \delta_E \rangle \equiv \langle f\left(\delta_M\right) \rangle , \tag{B.7}$$

where $\langle\rangle$ denotes ensemble average. Note that $f(\delta_M)$ is not only a function of δ_M, but also a function of ESNR γ and δ_T because the distribution of δ_M varies with them.

In practical phase retardation estimation, δ_T cannot be utilized as prior information, while ESNR can be obtained prior to the estimation directly from the measured OCT signals. Hence, we define a set of the suboptimal but practical transform function $f'(\delta_M)$, which is a polynomial function of δ_M and ESNR γ, but not a function of δ_T, as

$$f'(\delta_M; \gamma) = \sum_{i=0}^{n} b_i(\gamma)\, \delta_M^i, \tag{B.8}$$

where $b_i(\gamma)$ is i-th order polynomial coefficient of the transform function at an ESNR of γ.

In the design process of the transform function, $b_i(\gamma)$ is defined to be

$$\delta_T \simeq \langle \delta_E \rangle = \left\langle \sum_{i=0}^{n} b_i(\gamma)\, \delta_M^i \right\rangle . \tag{B.9}$$

To determine $b_i(\gamma)$ for a particular γ, δ_Ms were obtained by Monte-Carlo simulations for several δ_Ts from δ_T = 0 to π in steps of π/60. If $b_i(\gamma)$ is properly defined, the simulation results would follow the following 61 equations.

$$\begin{cases} 0 & \simeq & b_0(\gamma) & +b_1(\gamma)\,\langle \delta_{M,0} \rangle & +\cdots & b_n(\gamma)\left\langle \delta_{M,0}^n \right\rangle \\ \pi/60 & \simeq & b_0(\gamma) & +b_1(\gamma)\,\langle \delta_{M,\pi/60} \rangle & +\cdots & b_n(\gamma)\left\langle \delta_{M,\pi/60}^n \right\rangle \\ \vdots & & \vdots & \vdots & & \vdots \\ \pi & \simeq & b_0(\gamma) & +b_1(\gamma)\,\langle \delta_{M,\pi} \rangle & +\cdots & b_n(\gamma)\left\langle \delta_{M,\pi}^n \right\rangle \end{cases} , \tag{B.10}$$

where the left-hand-sides are the set true phase retardations δ_T, δ_{M,δ_T} is a raw phase retardation obtained by Monte-Carlo simulation with a set true phase retardation of δ_T, and n is the maximum polynomial order of $f'(\delta_M; \gamma)$. Here, each ensemble averaged value is obtained via Monte-Carlo simulation with 2^{21} trials; hence, they are known values. Equation (B.10) can also be written in a vector form as

$$\mathbf{D_T} \simeq \mathbf{D_M} \cdot \mathbf{B} \tag{B.11}$$

where $\mathbf{D_T} = [0, \pi/60, \cdots, \delta_T, \cdots, \pi]^T$, $\mathbf{B} = [b_0(\gamma), \cdots, b_n(\gamma)]^T$ and

$$\mathbf{D_M} = \begin{bmatrix} \left\langle \delta_{M,0}^0 \right\rangle & \left\langle \delta_{M,0}^1 \right\rangle & \cdots & \left\langle \delta_{M,0}^n \right\rangle \\ \vdots & \vdots & & \vdots \\ \left\langle \delta_{M,\delta_T}^0 \right\rangle & \left\langle \delta_{M,\delta_T}^1 \right\rangle & \ddots & \left\langle \delta_{M,\delta_T}^n \right\rangle \\ \vdots & \vdots & & \vdots \\ \left\langle \delta_{M,\pi}^0 \right\rangle & \left\langle \delta_{M,\pi}^1 \right\rangle & \cdots & \left\langle \delta_{M,\pi}^n \right\rangle \end{bmatrix}. \tag{B.12}$$

And then, the polynomial coefficients $b_i(\gamma)$ are defined as

$$\mathbf{B} \equiv \mathbf{D_M}^+ \cdot \mathbf{D_T} \tag{B.13}$$

where $\mathbf{D_M}^+$ is the pseudo-inverse of $\mathbf{D_M}$, obtained by singular value decomposition.

Equation (B.13) is equivalent to obtaining optimal $b_i(\gamma)$ by a least squares method. Thus, $b_i(\gamma)$ is defined to minimize a squared-sum error defined as

$$R = \sum_{k=0}^{60} \left[\delta_{T,k} - \left(b_0 + b_1 \left\langle \delta_{M,k} \right\rangle + \cdots + b_n \left\langle \delta_{M,k}^n \right\rangle \right) \right]^2 \tag{B.14}$$

where $\delta_{T,k} = k\pi/60$ is the true phase retardation of the k-th configuration of the Monte-Carlo simulation and $\delta_{M,k}$ is the corresponding simulated value of the measured phase retardation.

A transform function $f'(\delta_M; \gamma)$ is now defined for particular γ. For practical applications of phase retardation measurement, $f'(\delta_M; \gamma)$ is defined for γ of 0 dB to 50 dB in steps of 1 dB.

This transform function can be utilized to correct the contrast of phase retardation tomography images. Further, to obtain a qualitative phase retardation value, one of standard estimators can be applied after this distribution transform. According to the assumption made in the design of the transform function, a mean estimator would be reasonable. In this paper, we denote this combination of the distribution transform and mean estimator as an MCB estimator.

B.3 Performance evaluation

The detailed performance of the MCB estimator was evaluated via Monte-Carlo simulations. Figure B.3 shows the estimated phase retardation at several ESNR and true phase retardations, where 2^{16} trials of Monte-Carlo simulation were performed for each configuration. The green curves were obtained using the MCB estimator with the 4th order transform function, and the red curves were obtained using a mean estimator, as discussed above. As shown in this figure, the MCB estimator gives reasonable estimation even with a low ESNR of around 5 dB, while a standard mean estimator suffers from a significant error, even at an ESNR of 20 dB.

For further understanding of this error property, the estimation error is plotted as a function of the true phase retardation and ESNR, as shown in Fig. B.4. Figures B.4(a) and (b) show

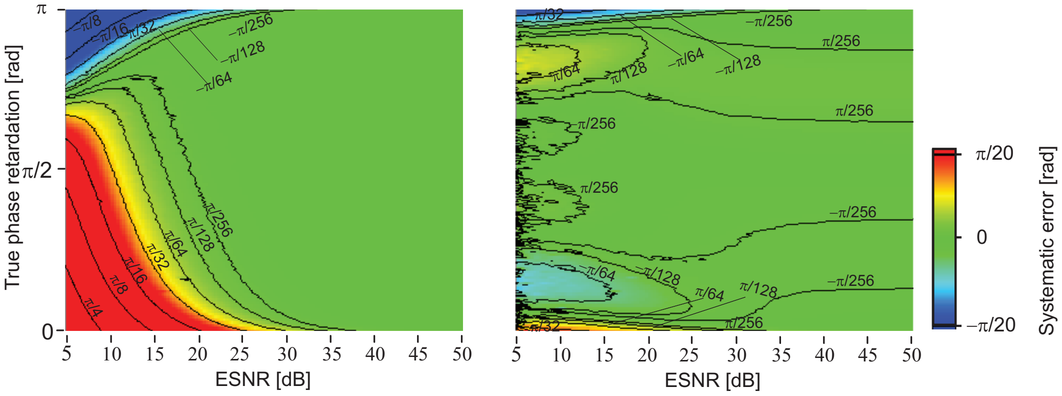

(a) (b)

Figure B.4: Contour plots of systematic error in mean estimator (a) and 4th order MCB estimator (b).

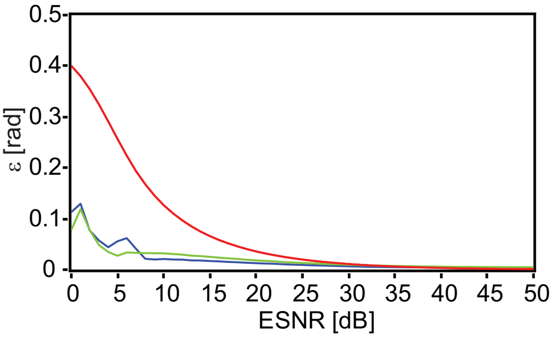

Figure B.5: Simulated precision of mean and MCB estimator for 2^{16} trials. The red, green, and blue curves represent the mean error energy corresponding to a mean estimator, 4th order MCB estimator, and 6th order MCB estimator, respectively.

the estimation error of mean estimator and 4th order MCB estimator, respectively. In these estimations, 2^{16} trials of δ_M or δ_E were averaged. Fig. B.4(a) clearly shows that the mean estimator includes a significant error if the true value is not close to 2.15 rad, and the error becomes larger as the true value approaches the perimeter of the measurement range of phase retardation, i.e. $[0, \pi]$. In contrast, the error is well controlled by the MCB estimator, as shown in Fig. B.4(b). When the ESNR is higher than 5 dB, the error is less than π/50 for most of the part of the plot. The maximum error is less than π/20 rad, which appears at $\delta_T = 0$ and π.

In order to evaluate the performance of the MCB estimator in a more qualitative manner, we defined a mean error energy, ε^2, as

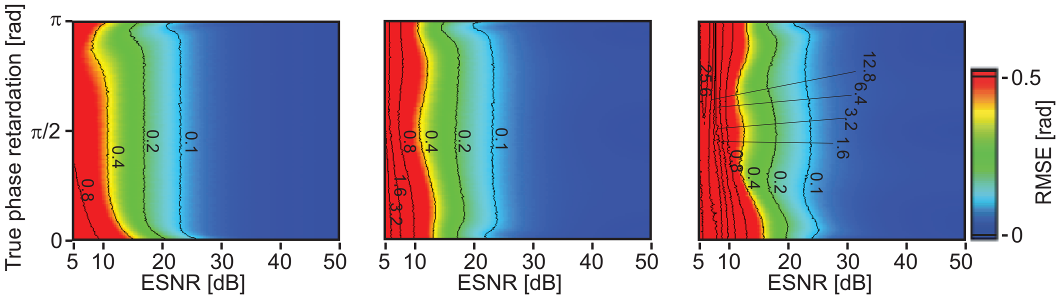

(a) (b) (c)

Figure B.6: Contour plots of RMSE in mean (a), 4th order MCB (b), and 6th order MCB estimator (c).

$$\varepsilon^2 = \left[\sum_{i=0}^{6} \left(\delta_{T,i} - \left\langle \delta_{M/E,i} \right\rangle \right)^2 \right] /7, \tag{B.15}$$

where $\delta_{T,i} = i\pi/6$ is true phase retardation and $\left\langle \delta_{M/E,i} \right\rangle$ is the ensemble mean of δ_M or δ_E when the true value is $\delta_{T,i}$. Figure B.5 shows the square-root of ε^2 as a function of $ESNR$, where ε was obtained via Monte-Carlo simulation with 2^{16} trials, followed by a mean estimator (red curve), 4th order MCB estimator (green curve), and 6th order MCB estimator (blue curve). For very high ESNR, e.g., higher than 25 dB, all the estimators provide a reasonably small amount of error. However, if the ESNR becomes lower than 25 dB, the error of the mean estimator increases rapidly, while the errors of the MCB estimators remain reasonably small until around 8 dB.

Thus far, we discussed the estimation error obtained with a sufficiently large number of trials. However, in practice, the number of trials/measurements we can perform at a single location is limited. Similarly, the kernel size of a local averaging filter that may be applied to a phase retardation image should be small. If the distribution of the transformed phase retardation is broad, i.e., randomeness is high, a large number of measurements are required to restrain the randomness of the result. Hence, the randomness of estimation is also of particular interest.

For qualitative evaluation, we define randomness as the root mean square error (RMSE) of the estimation as

$$\sigma = \sqrt{\langle (\delta_T - \delta_E)^2 \rangle}. \tag{B.16}$$

In Fig. B.6, σ is plotted as a function of ESNR and δ_T. We consider σ as a performance criterion of precision in estimation. Figures B.6 (a)-(c) show σ against δ_T and ESNR, where σ was obtained with mean, 4th order MCB, and 6th order MCB estimation, respectively. σ of all of these three methods increase as ESNR decreases. The 4th and 6th order MCB estimators possess a similar level of randomness if the ESNR is higher than 15 dB. However, the randomness in the 6th order MCB becomes significantly higher than that in the 4th order MCB if the ESNR is less

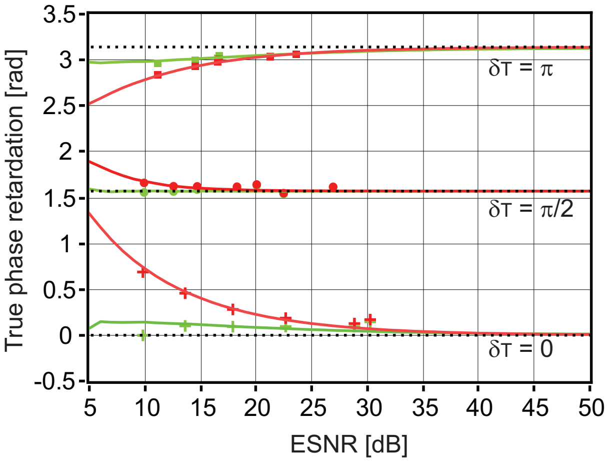

Figure B.7: Estimation result in simulation and experiment. The true values are denoted by black dashed lines, and the mean and MCB estimation results are denoted by red and green lines, respectively. The solid lines denote the mean of a 65536-trial estimation, and the squares, circles, and crosses denote 64-measurement estimations of a quarter wave-plate, one eighth wave-plate, and glass in the experiment.

than 10 dB. Therefore, we have used the 4th order transform function rather than a higher order transform function. In summary, the randomness in estimation increases as ESNR decreases, and the mean and higher order MCB generate the lowest and highest random error.

The experimental performance of the MCB estimator is quantitatively evaluated by measuring the phase retardations of a glass plate, a one-eighth wave-plate, and a quarter wave-plate, whose round trip phase retardations are 0, $\pi/2$, and π, respectively.

For this measurement, PS-SS-OCT with a 1.3 μm probe was employed. The details of the principle of this system are described in Ref. 52, and the details of the hardware configuration are described in Ref. 108. In short, this system has a depth resolution of 8.3 μm in air and a measurement speed of 30,000 A-lines/s. The measurements are performed with several ESNR configurations, which are controlled by a neutral density filter placed in front of the sample. For each ESNR configuration, 64 A-lines were successively obtained and utilized for the estimation.

The estimations are shown in Fig. B.7, where the red dots and green dots represent the estimations obtained by a mean estimator and MCB estimator, respectively. The red and green curves denote the corresponding estimations obtained by the Monte-Carlo simulations, and they are identical to those in Fig. B.3. The experiment is in good agreement with the Monte-Carlo simulation, and the MCB estimator enables better estimation than the mean estimator.

The estimation was not performed for ESNR less than 8 dB because of the difficulty in the experimental determination of ESNR, which arises from the non-uniform SNR of each detection channel of the PS-SS-OCT. Because the modulation efficiency of the source polarization of the system is not perfect, the SNR of the modulated channels are 8 to 10 dB lower than those of the non-modulated channels. The ESNR (γ), which is a significant parameter for the estimation, becomes unreliable in this low ESNR range; hence, δ_E also becomes unreliable.

The MCB estimator was applied to an *in vitro* chicken breast muscle, which is commonly utilized as a standard sample of PS-OCT evaluation. A 10-mm region on the sample was scanned to obtain a B-scan that consists of 512 A-lines. The B-scan measurements were successively performed 128 times at the same location on the sample; hence, 128 measurements were performed at a single point of an OCT image. Before applying the estimator, data points whose ESNR is lower than 8 dB were discarded because of their unreliability. The remaining data points were substituted by the mean and 4th order MCB estimators to form estimated-phase retardation images.

Figure B.8 shows the intensity image (a), ESNR image (b), a raw (non-avaraged) phase retardation image (c) and estimated phase retardation images formed by the mean estimator (d) and MCB estimator (e). Although the mean estimator significantly reduces the noise as shown in Figs. B.8(c) and (d), the contrast of the fringe shown in Fig. B.8(d) is still erroneously decreases in a deeper region. This is because, with low ESNR, the mean estimator underestimates the phase retardation when the true phase retardation is close to π, and overestimates the phase retardation when the true phase retardation is close to zero, as discussed above. On the other hand, the MCB estimator provides higher contrast of the fringe, as shown in Fig. B.8(e). It should be noted that with the MCB estimator, the fringe contrast decreases in a very deep region. This may be attributed to OCT signal crosstalk due to multiple scattering and the limitations of MCB.

The red dots in Figs. B.9(a)-(c) respectively show examples of depth resolved phase retardation signals extracted from a raw phase retardation image (a) and from phase retardation images obtained by the mean estimator (b) and the MCB estimator (c). The transversal locations of these signals are indicated by dashed lines in Figs. B.8(c)-(e). The dashed curves present corresponding depth-resolved ESNR signals in a logarithmic scale. The ESNR of Fig. B.9(a) is a non-averaged ESNR signal, while the ESNR of Figs. B.9(b)-(c) are averaged ESNR of A-lines which have been taken at the same location on the sample and been utilized for the estimation. It should be noted that the ESNR in the air is not 0 dB but around 3 dB because of the special calculation method.

The phase retardation is cumulative along depth; hence, a clear fringe pattern is observed in the estimated phase retardation by both methods. A clear decay was observed in the contrast of phase retardation fringe in the mean estimator image, caused by ESNR decreasing along the penetration depth; however, this did not happen in estimation using the MCB method.

As discussed above, the MCB estimator involves two steps, the distribution transform and ensemble mean operation. The distribution transform is a point-to-point function, i.e., the inputs of the distribution transform function are ESNR and δ_M of a single pixel, and the output is a single value of δ_E that is also associated with the single pixel. On the other hand, the mean operation requires multiple sampled values.

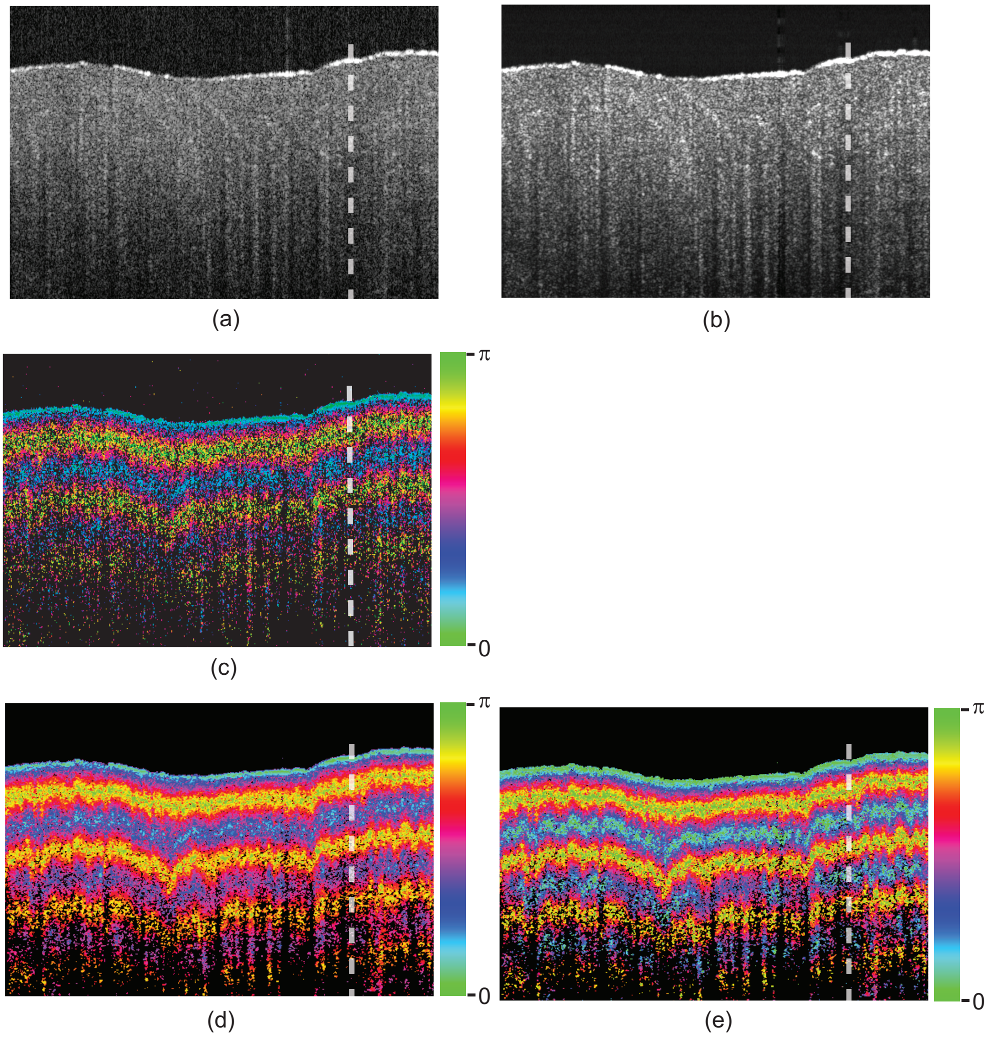

Figure B.8: B-scan images of *in vitro* chicken breast muscle. (a) is an intensity image, and (b) is a log-scaled $ESNR$ image. (c) is a single raw phase retardation image. (d) and (e) are phase retardation images obtained from mean and MCB estimators based on 128 B-scans. The white dashed lines denote the positions of the depth signal shown in Fig. B.9

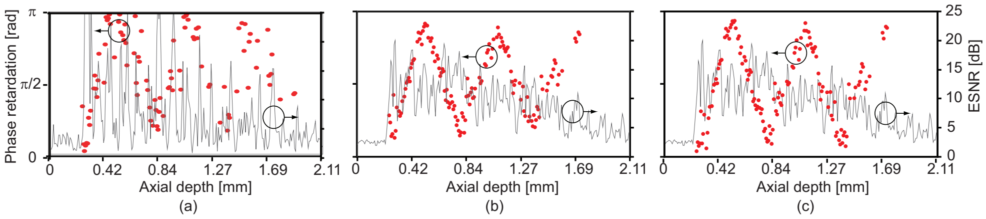

Figure B.9: Plots of A-line signals versus penetration depth. The red dots represent phase retardation values of raw phase retardation (a), obtained by mean estimator (b), and obtained by 4th order MCB estimator (c). Dashed curves represents corresponding ESNR values. The ESNR of (a) is a raw and non-averaged ESNR signal, while the ESNR of (b) and (c) are averaged ESNR of A-lines which have been taken at the same location on the sample and been utilized for the estimation.

Because of this property, the mean operation requires multiple phase retardation images measured at exactly the same location on the sample, while the distribution transform function requires only one image. This is an undesirable requirement for *in vivo* measurement.

This limitation can be overcome by three strategies. The first strategy is to apply only the transform function. This strategy is useful for qualitative observation; however, is not sufficient for quantitative assessment.

The second strategy is the use of the local mean as an alternative to the ensemble mean, in which the phase retardation values within a predefined special extent, known as a kernel, are averaged.

The third strategy is the use of slope fitting. Depth-oriented slope fitting of phase retardation has been widely utilized for the quantification of birefringence. [90, 101, 109] The slope fitting, i.e., least square linear fitting, is a maximum likelihood estimation with an assumption of symmetric distribution of noise, and the mean is a special case of linear fitting in which the slope is predefined as zero. Both the slope fitting and the mean are maximum likelihood estimations with the assumption of symmetric noise distribution; hence, the slope fitting would be applicable as an alternative to the mean operation. In the proposed scheme, the slope fitting of phase retardation is applied along the depth after the distribution transform. This would provide better estimation of birefringence of a biological specimen than the standard slope fitting without a distribution transform.

It is known that a similar systematic error exists in other PS-OCT algorithms including the widely utilized Hee's algorithm [43, 101]. Although the MCB estimator presented in this paper cannot be directly applied to other PS-OCT algorithms, it may be possible to design a tailored MCB estimator for the other algorithms by using Eqs. (B.11)-(B.13). In this designing process, the noise model of the PS-OCT should be properly customized for the PS-OCT algorithm of interest. Then, $\mathbf{D_M}$ of Eq. (B.13) is determined by a Monte-Carlo simulation, and $\mathbf{D_T}$ is defined by the simulation parameters.

In our Jones matrix PS-OCT, the SNR of each detection channel does not independently affect the error property; however, the ESNR γ dominates this property. Thus, $\mathbf{B}$ was determined for each γ value. However, this ESNR dependency is not warranted in other PS-OCT algorithms. The independent factors of the error property should be carefully considered in the design process.

B.4 Summary

In summary, this appendix proposed a nonlinear method to estimate a correct phase retardation value from raw phase retardation values measured via PS-OCT. This estimator involves of two operations, distribution transform and mean operation. The distribution transform function was designed to eliminate the asymmetric distribution of phase retardation, which causes a systematic error in the mean estimation of phase retardation. The transform function was designed on the basis of Monte-Carlo analysis of the error property of PS-OCT. The superior performance of the MCB estimator, as compared to that of a standard mean estimator, has been demonstrated by numerical simulations and experiments. The MCB estimator was also applied to an *in vitro* chicken breast muscle, and it showed higher contrast of the phase retardation fringe than a standard mean estimator. The distribution transform was applied to an *in vivo* human posterior eye, and a reasonable phase retardation image was obtained. MCB can potentially improve the phase retardation image quality of PS-OCT; moreover, it can further will enhance the ability of quantitative phase retardation measurement of PS-OCT.

Acknowledgements

First and foremost, I would like to express my sincere gratitude to my adviser, Dr. Yoshiaki Yasuno, for offering me a Ph.D candidate position in his group and supporting me with his best effort all through my Ph.D program. He also deserves special mention as someone who definitively promoted me in academic research by his immense knowledge and sagacious advice. I would also like to thank Prof. Masahide Itoh, my official adviser, for his kind and indispensable assistance during my Ph.D program.

I would like to thank other members of computational optics group in Univ. of Tsukuba for their help. Dr. Shuichi Makita's work provided basic theory to my first project. Data utilized in this research was obtained by systems developed Dr. Masahiro Yamanari, Youngjoo Hong, and Yiheng Lim. Dr. Jaillon Frank, Kazuhiro Kurokawa, and other members also contributed in my research by their helpful advice.

A special thanks goes to my parents living in my hometown in China. Their encourage has always been supporting me spiritually. I also thank all of my friends for their technical or spiritual assistance during my oversea life.

This study research partially supported by the Japan Science and Technology Agency through the contract of the development program of advanced measurement system, and a research grant from Tomey Corporation.

Bibliography

[1] D. Huang, E. A. Swanson, C. P. Lin, J. S. Schuman, W. G. Stinson, W. Chang, M. R. Hee, T. Flotte, K. Gregory, C. A. Puliafito, and J. G. Fujimoto, "Optical coherence tomography," Science **254**, 1178–1181 (1991).

[2] M. HEE, J. IZATT, E. SWANSON, D. HUANG, J. SCHUMAN, C. LIN, C. PULIAFITO, and J. FUJIMOTO, "OPTICAL COHERENCE TOMOGRAPHY OF THE HUMAN RETINA," ARCHIVES OF OPHTHALMOLOGY **113**(3), 325–332 (1995).

[3] A. Fercher, W. Drexler, C. Hitzenberger, and T. Lasser, "Optical coherence tomography - principles and applications," Rep. Prog. Phys. **66**(2), 239–303 (2003).

[4] M. E. J. van Velthoven, D. J. Faber, F. D. Verbraak, T. G. van Leeuwen, and M. D. de Smet, "Recent developments in optical coherence tomography for imaging the retina," PROGRESS IN RETINAL AND EYE RESEARCH **26**(1), 57–77 (2007).

[5] W. Drexler and J. G. Fujimoto, "State-of-the-art retinal optical coherence tomography," PROGRESS IN RETINAL AND EYE RESEARCH **27**(1), 45–88 (2008).

[6] R. Leitgeb, C. Hitzenberger, and A. Fercher, "Performance of fourier domain vs. time domain optical coherence tomography," Opt. Express **11**, 889–894 (2003).

[7] M. Choma, M. Sarunic, C. Yang, and J. Izatt, "Sensitivity advantage of swept source and Fourier domain optical coherence tomography," Opt. Express **11**, 2183–2189 (2003).

[8] R. Huber, M. Wojtkowski, and J. Fujimoto, "Fourier Domain Mode Locking (FDML): A new laser operating regime and applications for optical coherence tomography," OPTICS EXPRESS **14**(8), 3225–3237 (2006).

[9] W. Wieser, T. Klein, D. C. Adler, F. Trepanier, C. M. Eigenwillig, S. Karpf, J. M. Schmitt, and R. Huber, "Extended coherence length megahertz FDML and its application for anterior segment imaging," BIOMEDICAL OPTICS EXPRESS **3**(10), 2647–2657 (2012).

[10] M. Wojtkowski, V. J. Srinivasan, T. H. Ko, J. G. Fujimoto, A. Kowalczyk, and J. S. Duker, "Ultrahigh-resolution, high-speed, Fourier domain optical coherence tomography and methods for dispersion compensation," Opt. Express **12**, 2404–2422 (2004).

[11] D. Cabrera, “A Review of Algorithms for Segmentation of Retinal Image Data Using Optical Coherence Tomography,” in *Image Segmentation*, P.-G. Ho, ed. (InTech, 2011).

[12] A. Unterhuber, B. Povazay, B. Hermann, H. Sattmann, A. Chavez-Pirson, and W. Drexler, “In vivo retinal optical coherence tomography at 1040 nm - enhanced penetration into the choroid,” Optics Express **13**(9), 3252–3258 (2005).

[13] Y. Yasuno, Y. Hong, S. Makita, M. Yamanari, M. Akiba, M. Miura, and T. Yatagai, “In vivo high-contrast imaging of deep posterior eye by 1-$/mu$m swept source optical coherence tomography andscattering optical coherence angiography,” Opt. Express **15**(10), 6121–6139 (2007).

[14] R. Motaghiannezam, D. M. Schwartz, and S. E. Fraser, “In Vivo Human Choroidal Vascular Pattern Visualization Using High-Speed Swept-Source Optical Coherence Tomography at 1060 nm,” Investigative Ophthalmology & Visual Science **53**(4), 2337–2348 (2012).

[15] R. A. Linsenmeier and L. Padnick-Silver, “Metabolic Dependence of Photoreceptors on the Choroid in the Normal and Detached Retina,” Invest. Ophth. Vis. Sci. **41**(10), 3117–3123 (2000).

[16] D.-Y. Yu and S. J. Cringle, “Oxygen Distribution and Consumption within the Retina in Vascularised and Avascular Retinas and in Animal Models of Retinal Disease,” Prog. Retin. Eye Res. **20**(2), 175–208 (2001).

[17] L. M. Parver, C. Auker, and D. O. Carpenter, “Choroidal blood flow as a heat dissipating mechanism in the macula,” Am. J. Ophthalmol. **89**(5), 641–646 (1980). PMID: 6769334.

[18] J. W. Kiel and W. A. van Heuven, “Ocular perfusion pressure and choroidal blood flow in the rabbit,” Invest. Ophth. Vis. Sci. **36**(3), 579 –585 (1995).

[19] K. Polak, A. Luksch, F. Berisha, G. Fuchsjaeger-Mayrl, S. Dallinger, and L. Schmetterer, “Altered Nitric Oxide System in Patients With Open-Angle Glaucoma,” Arch Ophthalmol **125**(4), 494–498 (2007).

[20] T. Kubota, J. B. Jonas, and G. O. Naumann, “Decreased choroidal thickness in eyes with secondary angle closure glaucoma. An aetiological factor for deep retinal changes in glaucoma?” British Journal of Ophthalmology **77**(7), 430–432 (1993).

[21] C. W. Spraul, G. E. Lang, and H. E. Grossniklaus, “Morphometric analysis of the choroid, Bruch’s membrane, and retinal pigment epithelium in eyes with age-related macular degeneration.” Invest. Ophth. Vis. Sci. **37**(13), 2724 –2735 (1996).

[22] F. John V, “In vivo near-infrared fluorescence imaging,” Current Opinion in Chemical Biology **7**(5), 626–634 (2003).

[23] M. Destro and C. A. Puliafito, “Indocyanine green videoangiography of choroidal neovascularization,” Ophthalmology **96**(6), 846–853 (1989). PMID: 2472588.

[24] D. GUYER, L. YANNUZZI, J. SLAKTER, J. SORENSON, A. HO, and D. ORLOCK, “DIGITAL INDOCYANINE GREEN VIDEOANGIOGRAPHY OF CENTRAL SEROUS CHORIORETINOPATHY,” ARCHIVES OF OPHTHALMOLOGY **112**(8), 1057–1062 (1994).

[25] D. Coleman, R. H. Silverman, A. Chabi, M. J. Rondeau, K. Shung, J. Cannata, and H. Lincoff, “High-resolution ultrasonic imaging of the posterior segment,” Ophthalmology **111**(7), 1344 – 1351 (2004).

[26] J. A. Izatt, M. R. Hee, E. A. Swanson, C. P. Lin, D. Huang, J. S. Schuman, C. A. Puliafito, and J. G. Fujimoto, “Micrometer-scale resolution imaging of the anterior eye in vivo with optical coherence tomography,” Archives of Ophthalmology **112**(12), 1584–1589 (1994). PMID: 7993214.

[27] J. G. Fujimoto, W. Drexler, J. S. Schuman, and C. K. Hitzenberger, “Optical Coherence Tomography (OCT) in Ophthalmology: Introduction,” Opt. Express **17**(5), 3978–3979 (2009).

[28] T. Klein, W. Wieser, C. M. Eigenwillig, B. R. Biedermann, and R. Huber, “Megahertz OC-T for ultrawide-field retinal imaging with a 1050nm Fourier domain mode-locked laser,” Opt. Express **19**(4), 3044–3062 (2011).

[29] W. Drexler, U. Morgner, F. X. Kärtner, C. Pitris, S. A. Boppart, X. D. Li, E. P. Ippen, and J. G. Fujimoto, “In vivo ultrahigh-resolution optical coherence tomography,” Opt. Lett. **24**(17), 1221–1223 (1999).

[30] A. Fercher, C. Hitzenberger, G. Kamp, and S. El-Zaiat, “Measurement of intraocular distances by backscattering spectral interferometry,” Opt. Commun. **117**(1-2), 43–48 (1995).

[31] J. F. de Boer, B. Cense, B. H. Park, M. C. Pierce, G. J. Tearney, and B. E. Bouma, “Improved signal-to-noise ratio in spectral-domain compared with time-domain optical coherence tomography,” Opt. Lett. **28**, 2067–2069 (2003).

[32] R. F. Spaide, H. Koizumi, and M. C. Pozonni, “Enhanced Depth Imaging Spectral-Domain Optical Coherence Tomography,” American Journal of Ophthalmology **146**(4), 496 – 500 (2008).

[33] T. Fujiwara, Y. Imamura, R. Margolis, J. S. Slakter, and R. F. Spaide, “Enhanced Depth Imaging Optical Coherence Tomography of the Choroid in Highly Myopic Eyes,” Am. J. Ophthalmol. **148**(3), 445–450 (2009).

[34] B. Považay, B. Hermann, A. Unterhuber, B. Hofer, H. Sattmann, F. Zeiler, J. E. Morgan, C. Falkner-Radler, C. Glittenberg, S. Blinder, and W. Drexler, "Three-dimensional optical coherence tomography at 1050 nm versus 800 nm in retinal pathologies: enhanced performance and choroidal penetration in cataract patients," Journal of Biomedical Optics **12**(4), 041211 (pages 7) (2007).

[35] D. M. de Bruin, D. L. Burnes, J. Loewenstein, Y. Chen, S. Chang, T. C. Chen, D. D. Esmaili, and J. F. de Boer, "In Vivo Three-Dimensional Imaging of Neovascular Age-Related Macular Degeneration Using Optical Frequency Domain Imaging at 1050 nm," Investigative Ophthalmology & Visual Science **49**(10), 4545–4552 (2008).

[36] V. J. Srinivasan, D. C. Adler, Y. Chen, I. Gorczynska, R. Huber, J. S. Duker, J. S. Schuman, and J. G. Fujimoto, "Ultrahigh-Speed Optical Coherence Tomography for Three-Dimensional and En Face Imaging of the Retina and Optic Nerve Head," Invest. Ophth. Vis. Sci. **49**(11), 5103–5110 (2008).

[37] Y. Yasuno, M. Miura, K. Kawana, S. Makita, M. Sato, F. Okamoto, M. Yamanari, T. Iwasaki, T. Yatagai, and T. Oshika, "Visualization of Sub-retinal Pigment Epithelium Morphologies of Exudative Macular Diseases by High-Penetration Optical Coherence Tomography," Invest. Ophth. Vis. Sci. **50**(1), 405–413 (2009).

[38] M. R. Hee, "Optical coherence tomography of the eye," Ph.D. thesis, MASSACHUSETTS INSTITUTE OF TECHNOLOGY (1997).

[39] S. J. Chiu, X. T. Li, P. Nicholas, C. A. Toth, J. A. Izatt, and S. Farsiu, "Automatic segmentation of seven retinal layers in SDOCT images congruent with expert manual segmentation," Opt. Express **18**(18), 19,413–19,428 (2010).

[40] I. Ghorbel, F. Rossant, I. Bloch, S. Tick, and M. Paques, "Automated segmentation of macular layers in OCT images and quantitative evaluation of performances," Pattern Recogn. **44**(8), 1590 – 1603 (2011).

[41] V. Kajić, M. Esmaeelpour, B. Považay, D. Marshall, P. L. Rosin, and W. Drexler, "Automated choroidal segmentation of 1060 nm OCT in healthy and pathologic eyes using a statistical model," Biomed. Opt. Express **3**(1), 86–103 (2012).

[42] J. de Boer, T. Milner, and J. Nelson, "Determination of the depth-resolved Stokes parameters of light backscattered from turbid media by use of polarization-sensitive optical coherence tomography," Opt. Lett. **24**(5), 300–302 (1999).

[43] M. R. Hee, D. Huang, E. A. Swanson, and J. G. Fujimoto, "Polarization-sensitive low-coherence reflectometer for birefringence characterization and ranging," J. Opt. Soc. Am. B **9**, 903–908 (1992).

[44] S. Jiao and L. V. Wang, “Jones-matrix imaging of biological tissues with quadruple-channel optical coherence tomography,” J. Biomed. Opt. **7**(3), 350–358 (2002).

[45] G. Yao and L. V. Wang, “Two-dimensional depth-resolved Mueller matrix characterization of biological tissue by optical coherence tomography,” Opt. Lett. **24**(8), 537–539 (1999).

[46] E. Götzinger, M. Pircher, and C. K. Hitzenberger, “High speed spectral domain polarization sensitive optical coherence tomography of the human retina,” Opt. Express **13**, 10,217–10,229 (2005).

[47] M. Yamanari, M. Miura, S. Makita, T. Yatagai, and Y. Yasuno, “Phase retardation measurement of retinal nerve fiber layer by polarization-sensitive spectral-domain optical coherence tomography and scanning laser polarimetry,” J. Biomed. Opt. **13**, 014,013 (2008).

[48] E. Götzinger, M. Pircher, W. Geitzenauer, C. Ahlers, B. Baumann, S. Michels, U. Schmidt-Erfurth, and C. K. Hitzenberger, “Retinal pigment epithelium segmentation by polarization sensitive optical coherence tomography,” Opt. Express **16**(21), 16,410–16,422 (2008).

[49] M. Pircher, E. Goetzinger, R. Leitgeb, and C. K. Hitzenberger, “Transversal phase resolved polarization sensitive optical coherence tomography,” Phys. Med. Biol. **49**, 1257–1263 (2004).

[50] M. Yamanari, Y. Lim, S. Makita, and Y. Yasuno, “Visualization of phase retardation of deep posterior eye by polarization-sensitive swept-sourceoptical coherence tomography with1-$/mu$m probe,” Opt. Express **17**(15), 12,385–12,396 (2009).

[51] M. Yamanari, S. Makita, V. D. Madjarova, T. Yatagai, and Y. Yasuno, “Fiber-Based Polarization-Sensitive Fourier Domain Optical Coherence Tomography using B-Scan-Oriented Polarization Modulation Method,” Opt. Express **14**(14), 6502–6515 (2006).

[52] M. Yamanari, S. Makita, and Y. Yasuno, “Polarization-sensitive swept-source optical coherence tomography with continuous source polarization modulation,” Opt. Express **16**(8), 5892–5906 (2008).

[53] S. Makita, M. Yamanari, and Y. Yasuno, “Generalized Jones matrix optical coherence tomography: performance and local birefringence imaging,” Opt. Express **18**(2), 854–876 (2010).

[54] Y. Lim, M. Yamanari, S. Fukuda, Y. Kaji, T. Kiuchi, M. Miura, T. Oshika, and Y. Yasuno, “Birefringence measurement of cornea and anterior segment by office-based polarization-sensitive optical coherence tomography,” Biomed. Opt. Express **2**(8), 2392–2402 (2011).

[55] Q. Yang, C. A. Reisman, Z. Wang, Y. Fukuma, M. Hangai, N. Yoshimura, A. Tomidokoro, M. Araie, A. S. Raza, D. C. Hood, and K. Chan, "Automated layer segmentation of macular OCT images using dual-scale gradient information," Opt. Express **18**(20), 21,293–21,307 (2010).

[56] A. Mishra, A. Wong, K. Bizheva, and D. A. Clausi, "Intra-retinal layer segmentation in optical coherence tomography images," Opt. Express **17**(26), 23,719–23,728 (2009).

[57] M. Mujat, B. H. Park, B. Cense, T. C. Chen, and J. F. de Boer, "Autocalibration of spectral-domain optical coherence tomography spectrometers for in vivo quantitative retinal nerve fiber layer birefringence determination," Journal of Biomedical Optics **12**, 041205 (pages 6) (2007).

[58] S. Makita, Y. Hong, M. Yamanari, T. Yatagai, and Y. Yasuno, "Optical coherence angiography," Opt. Express **14**, 7821–7840 (2006).

[59] M. Baroni, P. Fortunato, and A. L. Torre, "Towards quantitative analysis of retinal features in optical coherence tomography," Med. Eng. Phys. **29**(4), 432 – 441 (2007).

[60] Y. Yasuno, M. Yamanari, K. Kawana, M. Miura, S. Fukuda, S. Makita, S. Sakai, and T. Oshika, "Visibility of trabecular meshwork by standard and polarization-sensitive optical coherence tomography," J. Biomed. Opt. **15**, 061,705 (2010).

[61] R. Margolis and R. F. Spaide, "A Pilot Study of Enhanced Depth Imaging Optical Coherence Tomography of the Choroid in Normal Eyes," American Journal of Ophthalmology **147**(5), 811 – 815 (2009).

[62] V. Manjunath, M. Taha, J. G. Fujimoto, and J. S. Duker, "Choroidal Thickness in Normal Eyes Measured Using Cirrus HD Optical Coherence Tomography," Am. J. Ophthalmol. **150**(3), 325 – 329.e1 (2010).

[63] G. Maguluri, M. Mujat, B. H. Park, K. H. Kim, W. Sun, N. V. Iftimia, R. D. Ferguson, D. X. Hammer, T. C. Chen, and J. F. de Boer, "Three dimensional tracking for volumetric spectral-domain optical coherence tomography," Opt. Express **15**(25), 16,808–16,817 (2007).

[64] M. Pircher, E. Götzinger, H. Sattmann, R. A. Leitgeb, and C. K. Hitzenberger, "In vivo investigation of human cone photoreceptors with SLO/OCT in combination with 3D motion correction on a cellular level," Opt. Express **18**(13), 13,935–13,944 (2010).

[65] L. Duan, S. Makita, M. Yamanari, Y. Lim, and Y. Yasuno, "Monte-Carlo-based phase retardation estimator for polarization sensitive optical coherence tomography," Opt. Express **19**(17), 16,330–16,345 (2011).

[66] R. A. Linsenmeier and L. Padnick-Silver, “Metabolic Dependence of Photoreceptors on the Choroid in the Normal and Detached Retina,” Investigative Ophthalmology & Visual Science **41**(10), 3117–3123 (2000).

[67] D. L. Nickla and J. Wallman, “The multifunctional choroid,” Progress in Retinal and Eye Research **29**(2), 144 – 168 (2010).

[68] R. J. Klein, C. Zeiss, E. Y. Chew, J.-Y. Tsai, R. S. Sackler, C. Haynes, A. K. Henning, J. P. SanGiovanni, S. M. Mane, S. T. Mayne, M. B. Bracken, F. L. Ferris, J. Ott, C. Barnstable, and J. Hoh, “Complement Factor H Polymorphism in Age-Related Macular Degeneration,” Science **308**(5720), 385–389 (2005).

[69] S. Alam, R. J. Zawadzki, S. Choi, C. Gerth, S. S. Park, L. Morse, and J. S. Werner, “Clinical Application of Rapid Serial Fourier-Domain Optical Coherence Tomography for Macular Imaging,” Ophthalmology **113**(8), 1425 – 1431 (2006).

[70] V. Manjunath, J. Goren, J. G. Fujimoto, and J. S. Duker, “Analysis of Choroidal Thickness in Age-Related Macular Degeneration Using Spectral-Domain Optical Coherence Tomography,” American Journal of Ophthalmology **152**(4), 663 – 668 (2011).

[71] L. YANNUZZI, K. ROHRER, L. TINDEL, R. SOBEL, M. COSTANZA, W. SHIELDS, and E. ZANG, “FLUORESCEIN ANGIOGRAPHY COMPLICATION SURVEY,” OPHTHALMOLOGY **93**(5), 611–617 (1986).

[72] M. HOPEROSS, L. YANNUZZI, E. GRAGOUDAS, D. GUYER, J. SLAKTER, J. SORENSON, S. KRUPSKY, D. ORLOCK, and C. PULIAFITO, “ADVERSE REACTIONS DUE TO INDOCYANINE GREEN,” OPHTHALMOLOGY **101**(3), 529–533 (1994).

[73] E. C. Lee, J. F. de Boer, M. Mujat, H. Lim, and S. H. Yun, “In vivo optical frequency domain imaging of human retina and choroid,” Opt. Express **14**(10), 4403–4411 (2006).

[74] L. Duan, M. Yamanari, and Y. Yasuno, “Automated phase retardation oriented segmentation of chorio-scleral interface by polarization sensitive optical coherence tomography,” Opt. Express **20**(3), 3353–3366 (2012).

[75] T. Torzicky, M. Pircher, S. Zotter, M. Bonesi, E. Götzinger, and C. K. Hitzenberger, “Automated measurement of choroidal thickness in the human eye by polarization sensitive optical coherence tomography,” Opt. Express **20**(7), 7564–7574 (2012).

[76] Y.-J. Hong, S. Makita, F. Jaillon, M. J. Ju, E. J. Min, B. H. Lee, M. Itoh, M. Miura, and Y. Yasuno, “High-penetration swept source Doppler optical coherence angiography by fully numerical phase stabilization,” Opt. Express **20**(3), 2740–2760 (2012).

[77] F. Jaillon, S. Makita, and Y. Yasuno, “Variable velocity range imaging of the choroid with dual-beam optical coherence angiography,” Opt. Express **20**(1), 385–396 (2012).

[78] P. Jirarattanasopa, S. Ooto, I. Nakata, A. Tsujikawa, K. Yamashiro, A. Oishi, and N. Yoshimura, “Choroidal Thickness, Vascular Hyperpermeability, and Complement Factor H in Age-Related Macular Degeneration and Polypoidal Choroidal Vasculopathy,” Investigative Ophthalmology & Visual Science **53**(7), 3663–3672 (2012).

[79] J.-C. Mwanza, F. E. Sayyad, and D. L. Budenz, “Choroidal Thickness in Unilateral Advanced Glaucoma,” Investigative Ophthalmology & Visual Science **53**(10), 6695–6701 (2012).

[80] J.-C. Mwanza, J. T. Hochberg, M. R. Banitt, W. J. Feuer, and D. L. Budenz, “Lack of Association between Glaucoma and Macular Choroidal Thickness Measured with Enhanced Depth-Imaging Optical Coherence Tomography,” Investigative Ophthalmology & Visual Science **52**(6), 3430–3435 (2011).

[81] Z. Yin, Vaegan, T. Millar, P. Beaumont, and S. Sarks, “Widespread choroidal insufficiency in primary open-angle glaucoma,” JOURNAL OF GLAUCOMA **6**(1), 23–32 (1997).

[82] M. Martínez-Pérez, A. Hughes, A. Stanton, S. Thom, A. Bharath, and K. Parker, “Retinal Blood Vessel Segmentation by Means of Scale-Space Analysis and Region Growing,” in *Medical Image Computing and Computer-Assisted Intervention łMICCAIł9*, C. Taylor and A. Colchester, eds., vol. 1679 of *Lecture Notes in Computer Science*, pp. 90–97 (Springer Berlin Heidelberg, 1999).

[83] J. Staal, M. Abramoff, M. Niemeijer, M. Viergever, and B. van Ginneken, “Ridge-based vessel segmentation in color images of the retina,” Medical Imaging, IEEE Transactions on **23**(4), 501 –509 (2004).

[84] L. Zhang, K. Lee, M. Niemeijer, R. F. Mullins, M. Sonka, and M. D. Abrmoff, “Automated Segmentation of the Choroid from Clinical SD-OCT,” Investigative Ophthalmology & Visual Science **53**(12), 7510–7519 (2012).

[85] V. Kajić, M. Esmaeelpour, C. Glittenberg, M. F. Kraus, J. Honegger, R. Othara, S. Binder, J. G. Fujimoto, and W. Drexler, “Automated three-dimensional choroidal vessel segmentation of 3D 1060 nm OCT retinal data,” Biomed. Opt. Express **4**(1), 134–150 (2013).

[86] M. Sohrab, K. Wu, and A. A. Fawzi, “A Pilot Study of Morphometric Analysis of Choroidal Vasculature ¡italic¿In Vivo¡/italic¿, Using En Face Optical Coherence Tomography,” PLoS ONE **7**(11), e48,631 (2012).

[87] J. Kittler, J. Illingworth, and J. Fglein, “Threshold selection based on a simple image statistic,” Computer Vision, Graphics, and Image Processing **30**(2), 125 – 147 (1985).

[88] N. Sang, H. Li, W. Peng, and T. Zhang, "Knowledge-based adaptive thresholding segmentation of digital subtraction angiography images," Image and Vision Computing **25**(8), 1263 – 1270 (2007).

[89] C.-H. Wu, G. Agam, and P. Stanchev, "A general framework for vessel segmentation in retinal images," in *Computational Intelligence in Robotics and Automation, 2007. CIRA 2007. International Symposium on*, pp. 37 –42 (2007).

[90] B. H. Park, C. Saxer, S. M. Srinivas, J. S. Nelson, and J. F. de Boer, "*In vivo* burn depth determination by high-speed fiber-based polarization sensitive optical coherence tomography," J. Biomed. Opt. **6**, 474–479 (2001).

[91] Y. Hori, Y. Yasuno, S. Sakai, M. Matsumoto, T. Sugawara, V. Madjarova, M. Yamanari, S. Makita, T. Yasui, T. Araki, M. Itoh, and T. Yatagai, "Automatic characterization and segmentation of human skin using three-dimensional optical coherence tomography," Opt. Express **14**, 1862–1877 (2006).

[92] S. Sakai, M. Yamanari, A. Miyazawa, M. Matsumoto, N. Nakagawa, T. Sugawara, K. Kawabata, T. Yatagai, and Y. Yasuno, "In vivo three-dimensional birefringence analysis shows collagen differences between young and old photo-aged human skin," J. Invest. Dermatol. **128**(7), 1641–1647 (2008).

[93] S. Sakai, N. Nakagawa, M. Yamanari, A. Miyazawa, Y. Yasuno, and M. Matsumoto, "Relationship between dermal birefringence and the skin surface roughness of photoaged human skin," J. Biomed. Opt. **14**(4), 044032 (pages 8) (2009).

[94] W. Drexler, D. Stamper, C. Jesser, X. Li, C. Pitris, K. Saunders, S. Martin, M. Lodge, J. Fujimoto, and M. Brezinski, "Correlation of collagen organization with polarization sensitive imaging of in vitro cartilage: Implications for osteoarthritis," Journal of Rheumatology **28**(6), 1311–1318 (2001).

[95] A. Baumgartner, S. Dichtl, C. Hitzenberger, H. Sattmann, B. Robl, A. Moritz, Z. Fercher, and W. Sperr, "Polarization-sensitive optical coherence tomography of dental structures," Caries Research **34**(1), 59–69 (2000).

[96] Y. Yasuno, M. Yamanari, K. Kawana, T. Oshika, and M. Miura, "Investigation of post-glaucoma-surgery structures by three-dimensional and polarization sensitive anterior eye segment optical coherence tomography," Opt. Express **17**(5), 3980–3996 (2009).

[97] F. Fanjul-Velez, M. Pircher, B. Baumann, E. Goetzinger, C. K. Hitzenberger, and J. L. Arce-Diego, "Polarimetric analysis of the human cornea measured by polarization-sensitive optical coherence tomography," J. Biomed. Opt. **15**(5) (2010).

[98] B. Cense, T. Chen, B. Park, M. Pierce, and J. de Boer, "Thickness and birefringence of healthy retinal nerve fiber layer tissue measured with polarization-sensitive optical coherence tomography," Invest. Ophthalmol. Vis. Sci. **45**(8), 2606–2612 (2004).

[99] M. Miura, M. Yamanari, T. Iwasaki, A. E. Elsner, S. Makita, T. Yatagai, and Y. Yasuno, "Imaging polarimetry in age-related macular degeneration," Invest. Ophthalmol. Vis. Sci. **49**(6), 2661–2667 (2008).

[100] M. Pircher, E. Gotzinger, O. Findl, S. Michels, W. Geitzenauer, C. Leydolt, U. Schmidt-Erfurth, and C. K. Hitzenberger, "Human Macula Investigated In Vivo with Polarization-Sensitive Optical Coherence Tomography," Invest. Ophthalmol. Vis. Sci. **47**, 5487–5494 (2006).

[101] M. Everett, K. Schoenenberger, B. Colston, and L. Da Silva, "Birefringence Characterization of Biological Tissue by Use of Optical Coherence Tomography," Opt. Lett. **23**(3), 228–230 (1998).

[102] L. V. Wang, "Mechanisms of Ultrasonic Modulation of Multiply Scattered Coherent Light: a Monte Carlo Model," Opt. Lett. **26**(15), 1191–1193 (2001).

[103] G. Yao and L. V. Wang, "Propagation of polarized light in turbid media: simulated animation sequences," Opt. Express **7**(5), 198–203 (2000).

[104] S.-P. Lin, L. Wang, S. L. Jacques, and F. K. Tittel, "Measurement of tissue optical properties by the use of oblique-incidence optical fiber reflectometry," Appl. Opt. **36**(1), 136–143 (1997).

[105] Z. Xie, L. V. Wang, and H. F. Zhang, "Optical fluence distribution study in tissue in dark-field confocal photoacoustic microscopy using a modified Monte Carlo convolution method," Appl. Opt. **48**(17), 3204–3211 (2009).

[106] D. Smithies, T. Lindmo, Z. Chen, J. Nelson, and T. Milner, "Signal attenuation and localization in optical coherence tomography studied by Monte Carlo simulation," Phys. Med. Biol. **43**(10), 3025–3044 (1998).

[107] S.-Y. Lu and R. A. Chipman, "Homogeneous and inhomogeneous Jones matrices," J. Opt. Soc. Am. A **11**(2), 766–773 (1994).

[108] Y. Lim, M. Yamanari, and Y. Yasuno, "Polarization sensitive corneal and anterior segment swept-source optical coherence tomography," Proc. SPIE **7550**, 75,500O (2010).

[109] W.-C. Kuo, N.-K. Chou, C. Chou, C.-M. Lai, H.-J. Huang, S.-S. Wang, and J.-J. Shyu, "Polarization-sensitive optical coherence tomography for imaging human atherosclerosis," Appl. Opt. **46**(13), 2520–2527 (2007).

Curriculum vitae

2003-2007	School of Life Science and Technology, Xi'an Jiaotong University, China
July 2007	B. E. in Biomedical Engineering, Xi'an Jiaotong University, China
2007-2010	Department of Physics, Tsinghua University, China
January 2010	M. S. in Physics, Tsinghua University, China
2010-present	Institute of Applied Physics, University of Tsukuba

Lian Duan was born on June 2nd, 1985 in China. He received B. E. in biomedical engineering from Xi'an Jiaotong University in 2007 and M. S. in physics from Tsinghua University in 2010. He started his Ph.D work in University of Tsukuba in 2010. His research was focused on the application of optical coherence tomography in ophthalmology.

Publications

As a first author

1. L. Duan, S. Makita, M. Yamanari, Y. Lim, and Y. Yasuno, "Monte-carlo-based phase retardation estimator for polarization sensitive optical coherence tomography," Opt. Express **19**, 16330–16345 (2011).

2. L. Duan, M. Yamanari, and Y. Yasuno, "Automated phase retardation oriented segmentation of chorio-scleral interface by polarization sensitive optical coherence tomography," Opt. Express **20**, 3353–3366 (2012).

As a coauthor

1. Y. Lim, Y. Hong, Y. Duan, and Y. Yasuno, "Passive Component Based Multi-Functional Jones Matrix Optical Coherence Tomography for Doppler and Polarization Sensitive Imaging of Retina," Opt. Lett. **37**, 1958–1960 (2012).

2. M. Yamanari, K. Ishii, S. Fukuda, Y. Lim, L. Duan, S. Makita, M. Miura, T. Oshika, and Y. Yasuno, "Optical Rheology of Porcine Sclera by Birefringence Imaging," Plos One **7**, 0044026 (2012).

Conference proceedings

1. L. Duan, M. Yamanari, and Y. Yasuno, “Automated detection of chorio-scleral interface using polarization-sensitive optical coherence tomography,” pp. 82131W–82131W–5 (2012).

Conferences

Oral presentations in domestic conferences

1. L. Duan, S. Makita, M. Yamanari, Y. Lim, and Y. Yasuno, “Monte Carlo Based Phase Retardation Estimator for Polarization Sensitive Optical Coherence Tomography,” Optics and Photonics Japan, 9pH9, Tokyo, November 2010.

2. L. Duan, M. Yamanari, and Y. Yasuno, “Automated segmentation of chorio-scleral interface using polarization sensitive optical coherence tomography,” Optics and Photonics Japan, 28aA3, Osaka, November 2011.

3. L. Duan, Y. Hong, and Y. Yasuno, “Classification of choroid based on blood vessel structure using high penetration optical coherence tomography,” Optics and Photonics Japan, 23aA2, Tokyo, October 2012.

Oral presentations in international conferences

1. L. Duan, S. Makita, M. Yamanari, Y. Lim, and Y. Yasuno, “Monte Carlo Based Phase Retardation Estimator for Polarization Sensitive Optical Coherence Tomography,” Photonics West, 7889-65, San Francisco, California, USA, January 2011.

2. L. Duan, M. Yamanari, and Y. Yasuno, “ Automated detection of chorio-scleral interface using polarization-sensitive optical coherence tomography,” Photonics West, 8213-67, San Francisco, California, USA, January 2012.

3. L. Duan, Y. Hong, M. Yamanari, Y. Lim, and Y. Yasuno, “Classification of choroid based on blood vessel structure using high penetration optical coherence tomography,” Photonics West, 8567-4, San Francisco, California, USA, February 2013.

Poster presentations in international conferences

1. L. Duan, S. Makita, M. Yamanari, Y. Lim, and Y. Yasuno, “Exact Phase Retardation Measurement Of Posterior Eye Using Polarization-sensitive Optical Coherence Tomography,” ARVO annual meeting, Program #4025, Poster # A163, Fort Lauderdale, Florida, USA, May 2011.

2. L. Duan, M. Yamanari, and Y. Yasuno, “Automated Segmentation Of Chorio-scleral Interface Using Polarization Sensitive Optical Coherence Tomography,” ARVO annual meeting, Program #4088, Poster # D1176, Fort Lauderdale, Florida, USA, May 2012.